Aerosol Responses to Precipitation Along North American Air Trajectories Arriving at Bermuda

Hossein Dadashazar[1], Majid Alipanah[2], Miguel Ricardo A. Hilario[3], Ewan Crosbie[4,5], Simon Kirschler[6,7], Hongyu Liu[8], Richard H. Moore[4], Andrew J. Peters[9], Amy Jo Scarino[4,5], Michael Shook[4], K. Lee Thornhill[4], Christiane Voigt[6,7], Hailong Wang[10], Edward Winstead[4,5], Bo Zhang[8], Luke Ziemba[4], Armin Sorooshian[1,3]

[1]Department of Chemical and Environmental Engineering, University of Arizona, Tucson, AZ, USA
[2]Department of Systems and Industrial Engineering, University of Arizona, Tucson, AZ, USA
[3]Department of Hydrology and Atmospheric Sciences, University of Arizona, Tucson, AZ, USA
[4]NASA Langley Research Center, Hampton, VA, USA
[5]Science Systems and Applications, Inc., Hampton, VA, USA
[6]Institute for Atmospheric Physics, DLR, German Aerospace Center, Oberpfaffenhofen, Germany
[7]Institute for Atmospheric Physics, University of Mainz, Mainz, Germany
[8]National Institute of Aerospace, Hampton, VA, USA
[9]Bermuda Institute of Ocean Sciences, 17 Biological Station, St. George's, GE01, Bermuda
[10]Atmospheric Sciences and Global Change Division, Pacific Northwest National Laboratory, Richland, WA, USA

*Correspondence to: Hossein Dadashazar (hosseind@arizona.edu)

Abstract

North American pollution outflow is ubiquitous over the western North Atlantic Ocean, especially in winter, making this location a suitable natural laboratory for investigating the impact of precipitation on aerosol particles along air mass trajectories. We take advantage of observational data collected at Bermuda to seasonally assess the sensitivity of aerosol mass concentrations and volume size distributions to accumulated precipitation along trajectories (APT). The mass concentration of particulate matter with aerodynamic diameter less than 2.5 μm normalized by the enhancement of carbon monoxide above background ($PM_{2.5}/\Delta CO$) at Bermuda was used to estimate the degree of aerosol loss during transport to Bermuda. Results for December-February (DJF) show most trajectories come from North America and have the highest APTs, resulting in significant reduction (by 53%) in $PM_{2.5}/\Delta CO$ under high APT conditions (> 13.5 mm) relative to low APT conditions (< 0.9 mm). Moreover, $PM_{2.5}/\Delta CO$ was most sensitive to increases in APT up to 5 mm (-0.044 $\mu g\ m^{-3}\ ppbv^{-1}\ mm^{-1}$) and less sensitive to increases in APT over 5 mm. While anthropogenic $PM_{2.5}$ constituents (e.g., black carbon, sulfate, organic carbon) decrease with high APT, sea salt in contrast was comparable between high and low APT conditions owing to enhanced local wind and sea salt emissions in high APT conditions. The greater sensitivity of the fine mode volume concentrations (versus coarse mode) to wet scavenging is evident from AERONET volume size distribution data. A combination of GEOS-Chem model simulations of ^{210}Pb submicron aerosol tracer and its gaseous precursor ^{222}Rn reveal that (i) surface aerosol particles at Bermuda are most impacted by wet scavenging in winter/spring (due to large-scale precipitation) with a maximum in March, whereas convective scavenging plays a substantial role in summer; and (ii) North American ^{222}Rn tracer emissions contribute most to surface ^{210}Pb concentrations at Bermuda in winter (~75-80%), indicating that air masses arriving at Bermuda experience large-scale precipitation scavenging while traveling from North America. A case study flight from the ACTIVATE field campaign on 22 February 2020 reveals a significant reduction in aerosol number and volume concentrations during air mass transport off the U.S. East Coast associated with increased cloud fraction and precipitation. These results highlight the sensitivity of remote marine boundary layer aerosol characteristics to precipitation along trajectories, especially when the air mass source is continental outflow from polluted regions like the U.S. East Coast.

1. Introduction

Aerosol properties are difficult to characterize in remote marine regions owing to the scarcity of monitoring stations as compared to over land. Island observatories are critical resources to investigate long-range transport of aerosol particles and their associated properties (e.g., Silva et al., 2020). The western North Atlantic Ocean (WNAO) includes the island of Bermuda, which has a rich history of monitoring data for both surface and columnar aerosol characteristics, thus affording the opportunity to study how aerosol properties are impacted by different sources and processes along the transport of air masses to the site. Consequently, Bermuda has been the subject of decades of intense atmospheric science research (Sorooshian et al., 2020), as it is a receptor site for both North African dust (Chen and Duce, 1983) and anthropogenic outflow from both North America (Arimoto et al., 1992; Galloway et al., 1989; Moody et al., 2014; Corral et al., 2021) and Europe (Anderson et al., 1996; Cutter, 1993). North American outflow reaching Bermuda has been linked to appreciable levels of anthropogenic species (e.g., sulfate, lead, elemental carbon, ozone) (Wolff et al., 1986), more acidic rainfall as compared to other air mass sources (Jickells et al., 1982), and a significant reduction of sulfate levels in both aerosol and wet deposition samples in response to reduced SO_2 emissions in recent decades (Keene et al., 2014).

There have been extensive studies reporting on some aspect of air mass history, normally by calculating air parcel trajectories using transport and dispersion models, prior to arrival at Bermuda (Sorooshian et al., 2020 and references therein), including predominant circulation patterns impacting Bermuda at different times of the year (e.g., Miller and Harris, 1985; Veron et al., 1992). What remains uncertain is how precipitation along those trajectories impacts surface aerosol characteristics at Bermuda. Wet scavenging rates are very difficult to constrain over open ocean areas such as the WNAO (Kadko and Prospero, 2011) not only because of complexity of physical mechanisms in play but also scarce necessary field measurements. Overall, more work is warranted to better constrain wet scavenging of aerosol particles along trajectories as such studies are sparse not only for the WNAO but also for other regions (Tunved et al., 2013; Hilario et al., 2021). Arimoto et al. (1999) used aerosol radionuclide data in relation to airflow pattern information to conclude that pollutant transport to Bermuda is common from the northwest and that precipitation scavenging can be influential; their analysis of rain effects on nuclide activities were based on rain data collected at Bermuda without knowledge of precipitation transport history prior to arrival. While many studies have investigated how composition at Bermuda varies based on air mass trajectories (Miller and Harris, 1985; Cutter, 1993; Huang et al., 1996), the subject of how precipitation along those trajectories impact the resultant aerosol at Bermuda has not been adequately addressed but is motivated by past works (Moody and Galloway, 1988; Todd et al., 2003).

In their recent aerosol climatology study for Bermuda, Aldhaif et al. (2021) found the peculiar result that fine particulate pollution in the winter months (December-February) was reduced even though there was an enhanced number density of air mass back trajectories traced back to North America. They hypothesized that enhanced seasonal cloud fractions and precipitation in winter (Painemal et al., 2021) contribute to the removal of aerosol particles during transport via wet scavenging, which we aim to study more deeply here using a variety of datasets. Results of this study have broad relevance to all remote marine regions impacted by transported continental pollution, in addition to advancing knowledge of how precipitation can impact surface aerosol characteristics.

2. Datasets and Methods

103   Datasets used in this work are summarized in Table 1 and described in brief detail below.
104
105 **Table 1. Summary of datasets used in this work. Data are between 1 January 2015 and 31**
106 **December 2019, with the exception of ACTIVATE aircraft data based on a single flight day**
107 **on 22 February 2020. Section 2 provides more details about the datasets used in this study,**
108 **including specific instruments from the ACTIVATE airborne dataset.**
109
110

Parameter	Acronym	Data Source	Spatial Resolution	Time Resolution
Particulate matter mass concentration (aerodynamic diameter less than 2.5 µm)	$PM_{2.5}$	Fort Prospect Station	-	Hourly
Particulate matter mass concentration (aerodynamic diameter less than 10 µm)	PM_{10}	Fort Prospect Station	-	Daily
Nitrogen monoxide concentration	NO	Fort Prospect Station	-	Hourly
Nitrogen dioxide concentration	NO_2	Fort Prospect Station	-	Hourly
Nitrogen oxide concentration	NO_X	Fort Prospect Station	-	Hourly
Volume size distribution	VSD	AERONET	-	Hourly
Carbon monoxide surface concentration	CO	MERRA-2	$0.625° \times 0.5°$	Hourly
Aerosol speciated surface mass concentrations	-	MERRA-2	$0.625° \times 0.5°$	Hourly
Surface wind speed	$Wind_{SF}$	MERRA-2	$0.625° \times 0.5°$	Hourly
Planetary boundary layer height	PBLH	MERRA-2	$0.625° \times 0.5°$	Hourly
Precipitation	APT/Rain	GDAS	$1° \times 1°$	Hourly
Aerosol/cloud properties	-	Airborne: ACTIVATE	-	1 – 45 Sec

111
112
113 **2.1 Bermuda Surface Measurements**
114   Aerosol and gas measurements were conducted at Fort Prospect in Bermuda (32.30° N,
115 64.77°W, 63 m ASL). Hourly $PM_{2.5}$ data were collected with a Thermo Scientific TEOM 1400a
116 Ambient Particulate Monitor with 8500C FDMS (Federal Equivalent Method EQPM-0609-181
117 for $PM_{2.5}$). Concentrations were determined by employing conditioned filter sample collection and
118 direct mass measurements using an inertial micro-balance (TEOM 1400a). Hourly precision was
119 $\pm 1.5\ \mu g\ m^{-3}$. Hourly data were averaged over 6 hour intervals to match the time frequency of the
120 trajectory data discussed subsequently. The conversion of hourly data to 6 hour data also helps to
121 mask, to some extent, the unwanted effects of local sources and processes that occur on a small
122 timescale.
123   PM_{10} concentrations were determined based on U.S. Environmental Protection Agency
124 (EPA) method IO-2 (EPA, 1999) using a Tisch model TE6070 hi-volume air sampler, equipped
125 with 8" × 10" TissuQuartz 2500 QAT-UP quartz fiber filters. The PM_{10} sampler was operated at a
126 flow rate of 2.1 m^3 min^{-1} yielding a total volume of 3000 m^3 over a 24 hr sampling period. The
127 sampler flow rate was calibrated every 3 months. Sampling was synchronized with the 1-in-6 day
128 national ambient air quality schedule used by EPA. Prior to deployment, the filters were
129 equilibrated for 24 hr in an environmental control chamber maintaining constant conditions of
130 relative humidity (35 ± 2%) and temperature (21 ± 2°C). The filters were then weighed with a
131 precision of ± 0.1 mg using a Mettler Toledo AB104 balance, which was modified for weighing
132 unfolded 8" × 10" filters, and then transferred to clean re-sealable plastic bags for transportation to

4

the field site. After sampling, the exposed filters were returned immediately to the laboratory where they were re-equilibrated in the environmental control chamber for 24 hr before being re-weighed to determine the particle loading from which particle concentrations were calculated. PM_{10} determinations have an accuracy of within $\pm$ 2.5%, which is equivalent to $\pm$ 0.2 µg m^{-3} based on the average of $PM_{2.5}$ between 2015 and 2019 (i.e., 6.7 µg m^{-3}).

Various gases were monitored with hourly time resolution using a Model T200U Trace-level NO/NO$_2$/NO$_x$ analyzer (Teledyne API), which is a U.S. EPA compliance analyzer relying on a proven chemiluminescence principle. The gas analyzer was routinely calibrated using NIST-certified calibrant NO$_2$ in ultra-high purity nitrogen (Airgas, Inc., Radnor Township, PA, USA). Acceptable criteria applied for single point quality control (QC) allows for $\pm$15.1% or $< \pm$1.5 ppb difference, whichever is greater (40 CFR Part 58 App A Sec. 3.1.1). Similar to $PM_{2.5}$, these hourly gas data were averaged to 6-hour resolution.

There were a few periods when data were missing with the longest one being between 11 January 2016 and 08 April 2016 for the gases, and also between 16 October 2017 and 20 January 2018 for $PM_{2.5}$. There was no major discontinuity in PM_{10} sampling. Table S1 reports the number of data points available for various seasons from the surface measurements at Fort Prospect in Bermuda.

Columnar aerosol data were obtained from a NASA AErosol RObotic NETwork (AERONET) (Holben et al., 1998) surface station at Tudor Hill (32.264° N, 64.879° W). Level 2 daily data have been quality assured and cloud screened based on the Version 3 algorithm (Giles et al., 2019). We focus on the volume size distribution (VSD) product that has 22 logarithmically equidistant discrete radii ranging from 0.05 to 15 µm. A radius of 0.6 µm typically discriminates between fine and coarse modes when using AERONET data (Dubovik et al., 2002; Schuster et al., 2006).

2.2 Reanalysis Data

Modern-Era Retrospective analysis for Research and Applications-Version 2 (MERRA-2) (Gelaro et al., 2017) products were used as a data source for speciated aerosol and gas parameters including surface mass concentration of sea-salt (collection "tavg1_2d_aer_Nx") and surface concentration of carbon monoxide (CO; collection "tavg1_2d_chm_Nx"). Surface wind speed and planetary boundary layer height (PBLH) (collection "tavg1_2d_flx_Nx") data were also obtained from MERRA-2. Hourly and 3-hourly data were downloaded and averaged for a 0.5° latitude by 0.625° longitude grid (i.e., 32° – 32.5°N and 64.375° – 65°W) surrounding Bermuda and subsequently averaged over 6-hour intervals to match the time frequency of trajectory analysis results. It should be noted that MERRA-2 data were temporally and spatially coincident with the ending point of trajectories over Bermuda. The Global Data Assimilation System (GDAS) one-degree archive data were used for trajectory calculations explained in the subsequent section. Precipitation data were also obtained along the trajectories based on GDAS one-degree data.

2.3 Air Mass Trajectory Analysis

To track air mass pathways arriving at Bermuda (32.30° N, 64.77°W), we obtained 10-day (240 hr) back-trajectories from the Hybrid Single-Particle Lagrangian Integrated Trajectory model (HYSPLIT) (Stein et al., 2015; Rolph et al., 2017). We used an ending altitude of 100 m (AGL) to be within the surface layer and close to the measurement site. As discussed later, sensitivity analysis with higher ending altitudes (500 m and 1 km; Figs. S1-S2) reveals similar results to using 100 m. Four trajectories were initialized (i.e., 6-hour interval) each day between 1 January 2015

00:00:00 UTC and 31 December 2019 18:00:00 UTC resulting in a total of 7304 individual trajectories. Trajectories were calculated using the GDAS one-degree archive data and with the "model vertical velocity" method, which means vertical motions were handled directly using meteorological data files. Moreover, accumulated precipitation along trajectories (APT) was calculated by integrating precipitation rate from GDAS, at the heights of trajectory endpoints, throughout the transport to the receptor site. Results presented in Figs. 1-3 are based on 10-day back-trajectories, whereas analyses presented in the remaining sections of the paper are based on 4-day (96 hr) back-trajectories.

Trajectory analyses contain errors that originate from factors including, but not limited to, the choice of input meteorological data, resolution of input data, and the vertical transport method used in trajectory calculations (Stohl et al., 1995; Cabello et al., 2008; Engström and Magnusson 2009). Although the choice of meteorological data is the most important contributor to the uncertainties associated with trajectories calculations (Gebhart et al., 2005), no particular dataset has been found to be superior in terms of yielding the lowest error. While in this study we used GDAS data, which have been widely used as input dataset for trajectory calculations even in regions with complicated topography (e.g., Tunved et al., 2013; Su et al., 2015), the aforementioned inherent errors should not be overlooked when interpreting the results presented in this work. Another factor that can contribute to the uncertainties for the results presented in this work is the use of GDAS as the source of precipitation data as previous works (Sun et al., 2018; Nogueira 2020) have demonstrated that there is some level of disagreement between precipitation datasets.

2.3.1 Concentration Weighted Trajectory Analysis and Seasonal Rain Maps

Concentration weighted trajectories (CWT) were calculated based on the 10-day back-trajectories from HYSPLIT in conjunction with Bermuda surface $PM_{2.5}$ data described in Section 2.1. The CWT method has been implemented widely to identify long-range pollutant transport pathways impacting a receptor site (Hsu et al., 2003; Wang et al., 2009; Hilario et al., 2020). Seasonal maps of average precipitation experienced by trajectories were also estimated based on 10-day back-trajectories from HYSPLIT. The aforementioned analyses were performed for $0.5°\times0.5°$ grids covering the area encompassed by 10°–80°N and 5°–170°W. A weight function (W_{ij} in Eq. 1) following the method of Dimitriou et al. (2015) was applied in the CWT analysis and precipitation maps to increase statistical stability. In Eq. 1, n_{avg} is the average number of trajectory end points per individual gird cell over the study region excluding cells with zero trajectory points and n_{ij} is the number of trajectory end points that lies in the grid cell (i,j).

$$W_{ij} = \begin{cases} 1 & n_{ij} > 3\,n_{avg} \\ 0.7 & 1.5\,n_{avg} < n_{ij} < 3\,n_{avg} \\ 0.4 & n_{avg} < n_{ij} < 1.5\,n_{avg} \\ 0.2 & n_{ij} < n_{avg} \end{cases} \qquad (1)$$

10-day back trajectories were implemented for generating CWT and rain maps to illustrate potential distant sources impacting Bermuda. But for more quantitative analyses presented in the subsequent sections focused on transport most relevant to the WNAO region, four-day back

trajectories were used by simply truncating 10-day trajectories. The use of four-day trajectories reduces the uncertainties associated with trajectory calculations in comparison to using 10-day trajectories and also enables us to focus on sources closer to the receptor site.

2.3.2 Trajectory Clustering

Hierarchical agglomerative clustering was used to identify characteristic trajectories reaching Bermuda at 100 m (AGL). Hierarchical clustering was based on the "complete linkage" method (Govender and Sivakumar, 2020). Four-day HYSPLIT back-trajectories were used to perform clustering analysis. Distances between trajectories were calculated using the Haversine formula, which calculates distance between two points on Earth assuming they are on a great circle (Sinnott, 1984). Clustering was performed for varying numbers of clusters, ranging between 2 and 32. The L-method (Kassomenos et al., 2010) was implemented to identify the optimum number of clusters. In this method, root mean square deviation (RMSD) was calculated for each clustering run and then plotted versus the number of clusters to determine the optimum solution. RMSDs were estimated based on the distances between trajectories and associated mean cluster trajectories.

2.4 Airborne Measurements

Airborne data from the Aerosol Cloud meteorology Interactions oVer the western ATlantic Experiment (ACTIVATE) are used from Research Flight 6 (RF6) on 22 February 2020. ACTIVATE involves two NASA Langley aircraft (HU-25 Falcon and UC-12 King Air) flying in coordination at different altitudes to simultaneously characterize the same vertical column with a focus on aerosol-cloud-meteorology interactions (Sorooshian et al., 2019). RF6 was a rare case of the HU-25 Falcon flying alone, but this aircraft conveniently included measurements relevant to this study. The ACTIVATE strategy involves the HU-25 Falcon flying in the boundary layer to characterize gas, aerosol, cloud, and meteorological parameters along the following level legs: Min. Alt. = lowest altitude flown (500 ft), BCB = below cloud base, ACB = above cloud base, BCT = below cloud top, ACT = above cloud top.

Data from the following instruments were used: Condensation Particle Counter (CPC; TSI Model 3772) for number concentration of particles with diameter > 10 nm; Scanning Mobility Particle Sizer (SMPS; TSI Model 3081) for aerosol size distribution data between 3.2 – 89.1 nm; Laser Aerosol Spectrometer (LAS; TSI Model 3340) for aerosol size distribution data between diameters of 0.09 – 5 µm; two-dimensional optical array imaging probe (2DS; SPEC Inc.) (Lawson et al., 2006) for rain water content (RWC) quantified by integrating rain drop size distributions between diameters of 39.9 – 1464.9 µm; and Fast Cloud Droplet Probe (FCDP; SPEC Inc.) (Knop et al., 2021) for cloud liquid water content (LWC) calculated by integrating drop size distributions between diameters of 3 – 50 µm. With the exception of SMPS data (45 second resolution), all airborne data were at 1 second resolution.

2.5 Radionuclide tracers in GEOS-Chem Model

Lead-210 (^{210}Pb, half-life 22.3 years) is the decay daughter of Radon-222 (^{222}Rn, half-life 3.8 days) emitted mainly from land surfaces. After production, it indiscriminately attaches to ambient submicron particles, which move with the air until being scavenged by precipitation or deposited to the surface. Because of its relatively well-known source and wet deposition as its principal sink, ^{210}Pb has long been used to test wet deposition processes in global models (e.g., Liu et al., 2001). It is also a useful tracer to describe continental air influence over oceans. In this study,

270   we use ^{210}Pb as simulated by the GEOS-Chem model to investigate the role of precipitation
271   scavenging in affecting seasonal surface aerosol concentrations at Bermuda.

272   GEOS-Chem (http://www.geos-chem.org) is a global 3-D chemical transport model driven
273   by meteorological fields from the Goddard Earth Observing System (GEOS) of the NASA Global
274   Modeling and Assimilation Office (Bey et al., 2001; Eastham et al., 2014). It has been widely used
275   to study trace gases and aerosols in the atmosphere. Here we use the model version 11-01
276   (http://wiki.seas.harvard.edu/geos-chem/index.php/GEOS-Chem_v11-01) driven by the MERRA-
277   2 reanalysis (at 2.5° longitude by 2° latitude resolution) to simulate [222]Rn and [210]Pb. The model
278   simulates the emission, transport (advection, convection, boundary layer mixing), deposition, and
279   decay of the radionuclide tracers (Liu et al., 2001; Brattich et al., 2017; Yu et al., 2018; Zhang et
280   al., 2021). As a function of latitude, longitude, and month, [222]Rn emission uses a customized
281   emission scenario that was built upon previous estimates and evaluated against global [222]Rn
282   surface observations and vertical profile measurements (Zhang et al., 2021). GEOS-Chem uses the
283   TPCORE advection algorithm of Lin and Rood (1996), calculates convective transport using
284   archived convective mass fluxes (Wu et al., 2007), and uses the non-local boundary-layer mixing
285   scheme implemented by Lin and McElroy (2010). The wet deposition scheme follows that of Liu
286   et al. (2001) and includes rainout (in-cloud scavenging) due to large-scale (stratiform and anvil)
287   precipitation, scavenging in convective updrafts, and washout (below-cloud scavenging) by
288   precipitation (Wang et al., 2011). A modification to the large-scale precipitation scavenging
289   scheme is included to use spatiotemporally varying cloud water contents from MERRA-2 instead
290   of a fixed constant value in the original model (Luo et al., 2019). Dry deposition is based on the
291   resistance-in-series scheme of Wesely (1989).
292
293   **3. Results and Discussion**
294   **3.1 Seasonal Profiles**
295   **3.1.1 Back-Trajectories**
296   Our results in Fig. 1 show that the summer months (June-August, JJA) are distinct due to
297   the Bermuda High promoting easterly winds at latitudes south of Bermuda that turn north and
298   become southwesterly (~ parallel to U.S. East Coast) towards Bermuda. The Bermuda high
299   pressure system and its associated anticyclonic circulation in the boundary layer have been
300   reported to be strongest in April–September (Merrill, 1994; Moody et al., 1995). This high pressure
301   system breaks down in other months in favor of strengthened extratropical subpolar low pressure,
302   thus yielding more air influence from the northwest and west (Arimoto et al., 1995; Davis et al.,
303   1997), which is clearly evident in the other three seasonal panels of Fig. 1 and most pronounced
304   in the winter months (December-February, DJF). In their analysis of air mass history leading to
305   rain events over Bermuda, Altieri et al. (2013) observed more influence from air originating over
306   water in warmer months (April–September) and faster moving air masses originating over the
307   continental U.S. primarily in the colder months of October–March. Moody and Galloway (1988)
308   also showed that cool months (October–March) were marked by more transport from the U.S. East
309   Coast. It can be deduced from Fig. 1 that based on the farther reaching source areas of the back-
310   trajectories in colder months, and especially DJF, that air moves faster in the boreal winter. Finally,
311   we note that Figs. S1-S2 show the same results as Fig. 1 but with ending altitudes of 500 m and 1
312   km over Bermuda; the sensitivity tests indicate the same general results and thus we continue the
313   discussion using results based on 100 m.
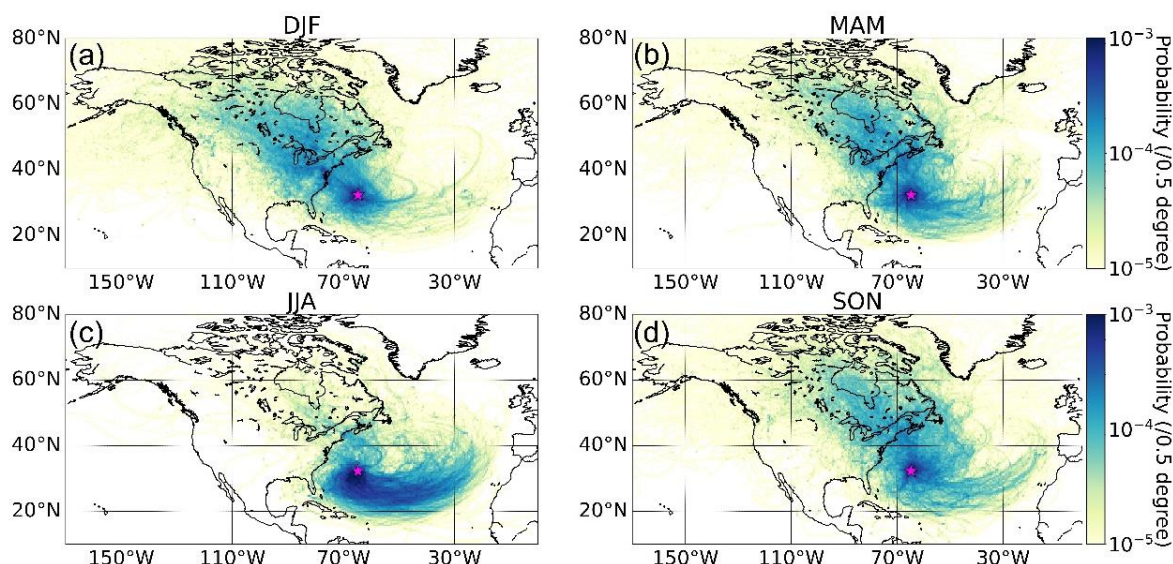
Figure 1. Seasonal maps (a-d) showing the probability density of trajectories calculated based on 10-day HYSPLIT backward trajectories reaching Bermuda (32.30° N, 64.77°W), denoted by the pink star, at 100 m (AGL). This analysis is based on trajectories between 01 January 2015 and 31 December 2019. Analogous results for ending altitudes of 500 m and 1 km are shown in Figs. S1 and S2, respectively.

3.1.2 Surface Aerosol and NO$_x$

Recent work has shown a seasonal cycle over Bermuda for column-integrated aerosol properties, with aerosol optical depth (AOD) being highest in March-May (MAM) and JJA and lowest in September-November (SON) and DJF (Aldhaif et al., 2021). They further showed that sea salt contributed more to AOD in the colder months (SON, DJF) whereas sulfate, organic carbon, black carbon and dust were more dominant in MAM and JJA. In their examination of aerosol type seasonality at Bermuda, Huang et al. (1999) observed that marine and crustal elements peaked in winter and summer, respectively, and that pollution-derived particles dominated in spring with a smaller peak in fall. We use data from Fort Prospect station to gain a revised perspective about seasonality and the weekly cycle of surface layer aerosol and additionally NO$_x$ (box notch plots in Figs. S3a-f).

Median seasonal concentrations of PM$_{2.5}$ (μg m^{-3}) were as follows at Bermuda, being largely consistent with the AOD seasonal cycle: DJF = 5.50, MAM = 6.36, JJA = 6.11, SON = 5.33 (Fig. S3). NO$_x$ exhibited a similar seasonal pattern (ppbv): DJF = 17.76, MAM = 21.62, JJA = 18.68, SON = 13.95 (Fig. S3). It is difficult to ascertain sources and impacts of precipitation on PM$_{2.5}$ based on these values. As a next step we present the seasonal CWT maps showing the predominant pathways accounting for the majority of PM$_{2.5}$ at Bermuda (Fig. 2). Expectedly, PM$_{2.5}$ in JJA is largely accounted for by trajectories following the general anticyclonic circulation already shown in Fig. 1c associated with the Bermuda High. These air masses are enriched with African dust as has been documented in many past studies (e.g., Arimoto, 2001; Huang et al., 1999; Muhs et al., 2012). In contrast, the other seasons (especially DJF and MAM) showed greater relative influence from North American outflow versus other source regions.
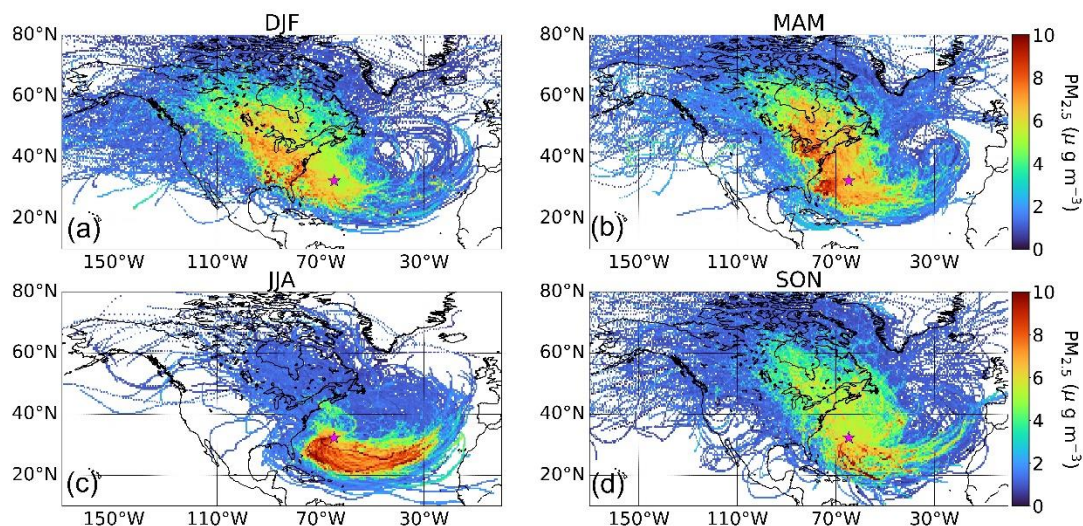
Figure 2. Seasonal (a-d) concentration-weighted trajectory maps (CWT) for PM$_{2.5}$ measured at Fort Prospect in Bermuda, denoted by the pink star. This analysis is based on trajectories between 1 January 2015 and 31 December 2019.

While we focus on long-range transport of PM$_{2.5}$ to Bermuda, local sources cannot be ignored, including both sea salt and non-sea salt species (e.g., Galloway et al., 1988). The island has a population of approximately 64,000 as of 2016 (Government of Bermuda, 2019). Local influence from anthropogenic sources has been reported to be insignificant in contrast to transported pollution (Galloway et al., 1988; Keene et al., 2014). We assess how significant local anthropogenic sources are based on day-of-week aerosol concentrations and whether significantly higher levels exist on working days as compared to weekend days as shown in other regions with strong anthropogenic influence (Hilario et al., 2020 and references therein). Our analysis found negligible difference between working days (Monday-Friday) and weekend days (Saturday-Sunday) for both PM$_{2.5}$ and NO$_x$ when analysis was done based on annual (Figs. S3b/d) or seasonal data (Figs. S4-S5). Therefore, it is less likely that local anthropogenic emissions dominate the island's PM$_{2.5}$ and NO$_x$, providing support for transported sources being more influential; as will be shown, normalizing PM$_{2.5}$ by CO helps control for local anthropogenic influence.

We also examined seasonal and day-of-week statistics for PM$_{10}$ to assess the relative importance of coarse aerosol types including mainly sea salt and dust (Figs. S3e-f). Results reveal the highest median PM$_{10}$ values (μg m^{-3}) in DJF (19.24), followed by MAM (18.51), JJA (17.98), and SON (15.88). As will be shown later and already documented (Aldhaif et al., 2021), surface wind speeds around Bermuda are highest in DJF, contributing to higher sea salt emissions. Expectedly there was no observable PM$_{10}$ weekly cycle as dust and sea salt are naturally emitted. Both PM$_{2.5}$ and PM$_{10}$ exhibited their highest seasonal standard deviations in JJA owing most likely to the episodic nature of some pollution events such as with dust and biomass burning (e.g., Aldhaif et al., 2021).

3.1.3 Precipitation Along Trajectories

372   Figure 3 shows seasonal profiles of average precipitation rate obtained from GDAS (Table
373   1) in 0.5°×0.5° grids based on 10-day back trajectories arriving at Bermuda (100 m AGL). The
374   spatiotemporal pattern of precipitation over the WNAO is of most interest in terms of potential
375   impacts on wet scavenging of aerosol during the transport of North American pollution to
376   Bermuda. In that regard, DJF shows the most pronounced levels of precipitation to the north and
377   northwest of Bermuda over the WNAO, coincident with strong and frequent convection linked to
378   frontogenesis (Painemal et al., 2021). This is consistent with how Painemal et al. (2021) showed
379   that precipitation exhibits maximum levels over the Gulf Stream path owing to relatively high sea
380   surface temperature and strong surface turbulent fluxes.
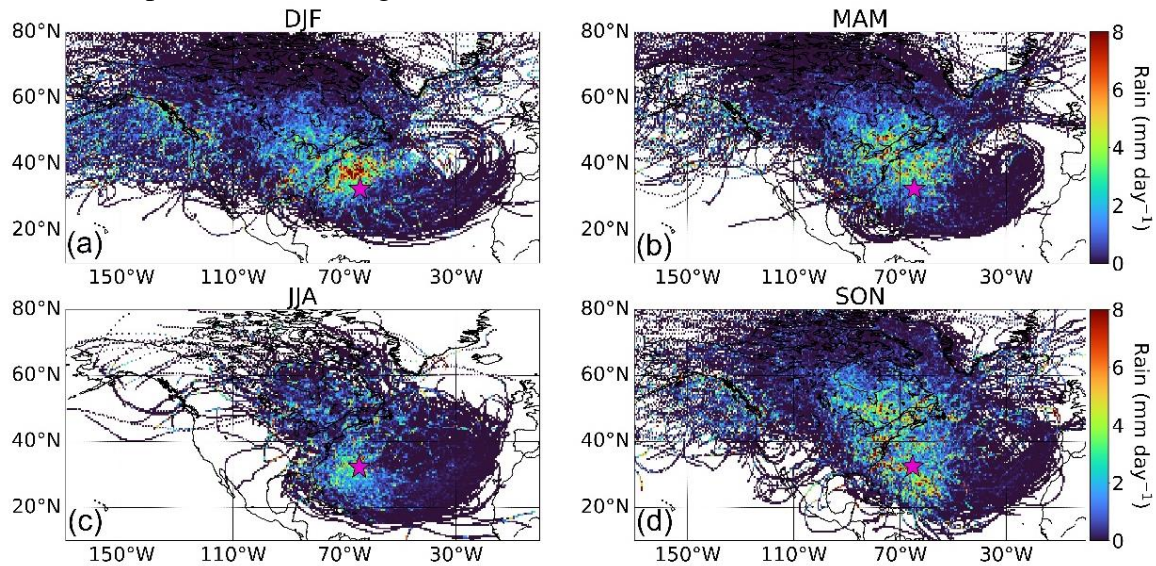
381
382 **Figure 3. Seasonal maps (a-d) of average precipitation occurring in 0.5°×0.5° grids based on**
383 **10-day backward trajectories reaching Bermuda (32.30° N, 64.77°W; pink star) at 100 m**
384 **(AGL). This analysis is based on trajectories between 1 January 2015 and 31 December 2019.**
385

386 **3.2 Trajectory Clustering**

387   Prior to examining how precipitation directly impacts $PM_{2.5}$ at Bermuda, we identify
388   characteristic trajectory pathways using the hierarchical agglomerative clustering method
389   described in Section 2.3.2. We reiterate that this analysis is based on 4 days of back-trajectories,
390   rather than 10 days from Figs. 1-3, to focus more on transport closer to Bermuda. The optimum
391   solution based on the L-method (see Section 2.3.2) resulted in eight trajectory clusters (Fig. 4a),
392   with five (numbered 1-5) coming from North America and the remaining three (numbered 6-8)
393   more characteristic of the anticyclonic circulation described already for JJA. The former five
394   clusters account for 49% of the total trajectories, with the latter three responsible for the remaining
395   51%. The majority of trajectories from North America come offshore north of North Carolina (i.e.,
396   coastal areas north of ~35°N) .
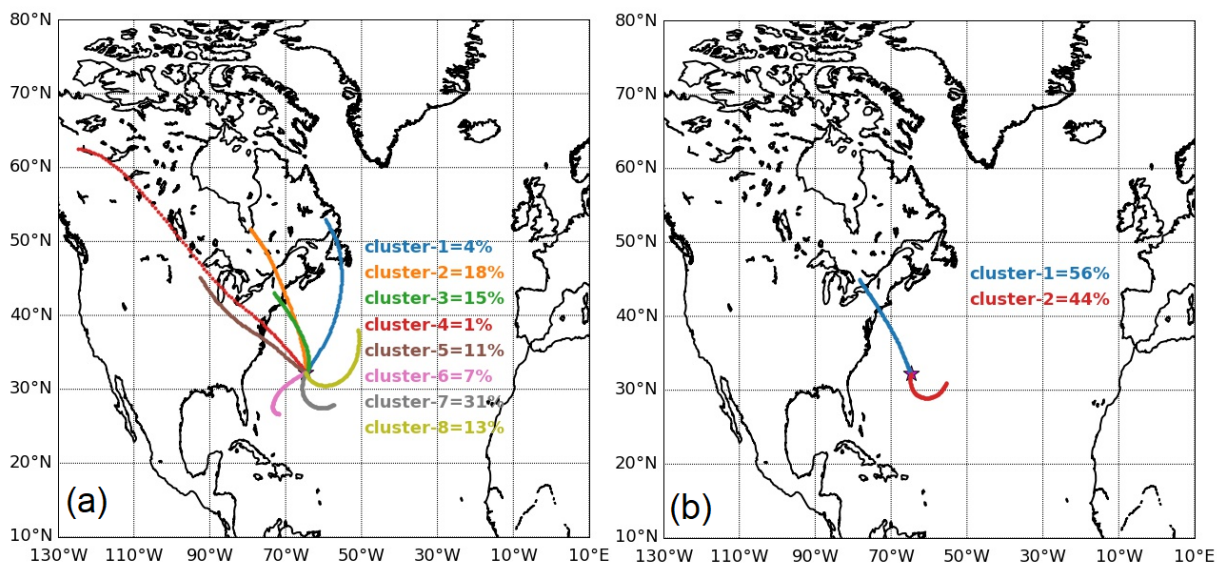
Figure 4. Cluster mean trajectories based on the (a) optimum solution having eight clusters and (b) a simplified solution with two clusters to enhance statistics for North American trajectories. Clustering was performed on four-day HYSPLIT backward trajectories between 1 January 2015 and 31 December 2019.

For the sake of simplicity of the remainder of the discussion, we reduced the number of characteristic trajectories to two (Fig. 4b), by conducting a new clustering analysis, to have one from North America and the other from the southeast. Using only two clusters increases the number of data points in the North American cluster for more robust calculations of rain-aerosol relationships. Our choice to put together all North American air mass clusters into one group is aligned with a similar clustering choice by Chen and Duce (1983; see their Fig. 3) where trajectories were grouped together from Florida to the Canadian maritime provinces. Also, Mead et al. (2013) divided trajectory data ending at Bermuda into "Saharan" and "non-Saharan" seasons that generally coincide with our division of data into two clusters. Cluster 1 from North America accounts for 56% of trajectories and Cluster 2 from the southeast is linked to 44% of trajectories. It is clear from the two clusters that the North American air masses generally move faster as the characteristic 4-day back-trajectories originate farther away from Bermuda than that of Cluster 2.

Regardless of season, Cluster 1 was associated with higher APT values with the seasonal median values (units of mm) as follows (Cluster1/Cluster 2): DJF = 6.1/2.3; MAM = 5.2/1.8; JJA = 6.7/2.8; SON = 7.0/5.1. Figure 5 shows a box notch plot comparing APT between clusters for each season, demonstrating statistically significant differences in median values between clusters for a given season at 95% confidence. Furthermore, Cluster 1 exhibited higher CO levels at Bermuda for each season with median values (units of ppbv) as follows (Cluster 1/Cluster 2): DJF =89.7/76.3; MAM = 88.5/75.0; JJA = 68.9/58.7; SON = 81.6/65.6. Therefore, the combination of pollution outflow from North America and higher APT values makes Cluster 1 more relevant in terms of identifying potential wet scavenging effects on transported aerosol over the WNAO. The remainder of the study thus focuses on Cluster 1.

12
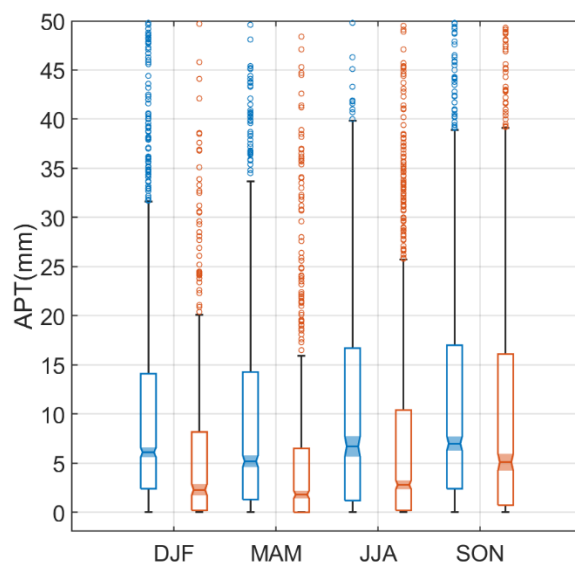
Figure 5. Box notch plot for each season comparing accumulated precipitation along trajectories (APT) for Clusters 1 (blue) and 2 (orange) from Fig. 4b. APT values were estimated from four-day HYSPLIT back trajectories reaching Bermuda (32.30° N, 64.77°W) at 100 m AGL. The middle, bottom, and top lines in each box represent the median, 25th percentile, and 75th percentile, respectively. Markers show extreme values identified based on 1.5×IQR (interquartile range) distance from the top of each box. Whiskers represent maximum and minimum values excluding extreme points. Boxes with notches and shaded regions that do not overlap have different medians at the 95% confidence level.

3.3 North America Trajectory Results

We next examine the relationship between APT and aerosol transport to Bermuda based on Cluster 1 results (Table 2). We compare data for "low" and "high" APT values based on thresholds being the 25th percentile (< 0.9 mm) and 75th percentile (> 13.5 mm), respectively, based on cumulative data from all seasons and years. As wet scavenging is expected to reduce $PM_{2.5}$ during its transport from North America to Bermuda, we anticipate lower $PM_{2.5}$ values at high APT. However, the results indicate this is only the case for MAM and JJA, with similar median values in SON and a higher median value in DJF for high APT conditions. Interestingly, NO, NO_2, NO_x, and CO were all significantly higher in DJF for high APT conditions too. This raises the issue that absolute $PM_{2.5}$ concentrations should be normalized to account for the differences in concentration that existed closer to North America prior to potential wet scavenging over the WNAO.

To study the effects of wet removal processes on aerosol particles during long-range transport to a receptor site, many studies have used aerosol concentrations normalized by the concentration of an inert gaseous species co-emitted with particles at distance sources. Such normalization is critical and superior to the use of only aerosol concentration as the latter can be influenced by local sources that can mask aerosol response to removal processes during long-range transport. CO exhibits three important traits qualifying it as a species to normalize $PM_{2.5}$ by: (i) a reliable marker of anthropogenic pollution stemming from North America (Corral et al., 2021); (ii) being relatively insensitive to wet scavenging processes; and (iii) having a long lifetime in the

13

455 atmosphere (~1 month; Weinstock, 1969) compared to aerosol particles. Consequently, we
456 normalize $PM_{2.5}$ by ΔCO to quantify transport efficiency and to reveal the potential effects of wet
457 scavenging as has been done in past studies for other regions (Park et al., 2005; Garrett et al., 2010;
458 Hilario et al., 2021; Matsui et al., 2011; Moteki et al., 2012; Oshima et al., 2012). We first
459 determine the 5th percentile value of surface CO at Bermuda for each season for Cluster 1
460 trajectories and assume those are the seasonal background values as done also by Matsui et al.
461 (2011). We then calculate ΔCO as the difference between each 6-hourly CO data point at Bermuda
462 and the background value for a given season. We only use data when $\Delta CO > 3.2$ ppbv to ensure a
463 sufficiently high signal to noise ratio (Garrett et al., 2010).
464
465 **Table 2. Seasonal medians of aerosol, gas, and meteorological variables for Cluster 1 divided**
466 **into high- and low-APT categories. Differences in median values that are statistically**
467 **significant (p-value < 0.05) based on a Wilcoxon rank-sum test are highlighted with bold and**
468 **italic font. Percentage differences[*] between high- and low-APT median values are provided**
469 **in parentheses. NO, NO_2, NO_x, and $PM_{2.5}$ are based on Fort Prospect measurements, whereas**
470 **all other parameters are from MERRA-2 with the exception of the two APT rows (derived**
471 **from HYSPLIT and GDAS) and the last 8 rows corresponding to AERONET volume size**
472 **distribution data. We combined all seasons for AERONET data to have sufficient statistics**
473 **for comparisons (high APT = 16 points, low APT = 19 points). AERONET parameters**
474 **include volume concentration (V), effective radii (R_{eff}), volume median radii (R), and**
475 **geometric standard deviation (σ) with subscripts f and c for fine and coarse modes,**
476 **respectively. Number of data points for each table entry is summarized in Table S2.**
477

478

Parameter	High-rain (APT > 13.5 mm)/Low-rain (APT < 0.9 mm) (% Difference[*])			
	DJF	MAM	JJA	SON
NO (ppbv)	*6.0/3.5 (71 %)*	7.3/7.8 (-6 %)	*8.3/13.1 (-37 %)*	3.8/4.2 (-10 %)
NO$_2$ (ppbv)	*13.9/12.8 (9 %)*	13.4/12.0 (12 %)	*8.6/6.6 (30 %)*	9.4/9.2 (2 %)
NO$_x$ (ppbv)	*19.6/17.5 (12 %)*	21.2/21.8 (-3 %)	*17.4/23.3 (-25 %)*	14.1/14.2 (-1 %)
CO (ppbv)	*97.8/84.7 (15 %)*	*92.4/88.6 (4 %)*	*70.8/65.9 (7 %)*	83.7/81.4 (3 %)
PM$_{2.5}$ (μg m^{-3})	*6.1/5.5 (11 %)*	*6.7/7.3 (-8 %)*	*5.9/7.8 (-24 %)*	5.5/5.1 (8 %)
PM$_{2.5}$/ΔCO (μg m^{-3} ppbv^{-1})	*0.29/0.62 (-53 %)*	*0.35/0.51 (-31 %)*	0.32/0.37 (-14 %)	0.27/0.33 (-18 %)
Sea-Salt (μg m^{-3})	*47.2/28.4 (66 %)*	*44.1/25.4 (74 %)*	27.0/26.0 (4 %)	*50.6/36.0 (41 %)*
Sea-Salt$_{PM2.5}$ (μg m^{-3})	*6.2/4.0 (55 %)*	*6.2/4.1 (51 %)*	4.9/4.9 (0 %)	*6.8/5.0 (36 %)*
Dust (μg m^{-3})	*0.80/0.91 (-12 %)*	*2.32/3.03 (-23 %)*	*4.47/3.02 (48 %)*	*1.16/1.04 (12 %)*
Dust$_{PM2.5}$ (μg m^{-3})	*0.31/0.34 (-9 %)*	*0.79/1.00 (-21 %)*	*1.58/1.18 (34 %)*	*0.44/0.36 (22 %)*
Sea-Salt/ΔCO (μg m^{-3} ppbv^{-1})	*2.10/2.74 (-23 %)*	*2.54/1.70 (49 %)*	1.50/1.58 (-5 %)	*2.44/1.66 (47 %)*
Sulfate/ΔCO (μg m^{-3} ppbv^{-1})	*0.029/0.055 (-47 %)*	*0.041/0.052 (-21 %)*	0.039/0.046 (-15 %)	0.024/0.027 (-11 %)
Dust/ΔCO (μg m^{-3} ppbv^{-1})	*0.038/0.082 (-54 %)*	*0.129/0.186 (-31 %)*	*0.235/0.152 (55 %)*	0.052/0.047 (11 %)
BC/ΔCO (μg m^{-3} ppbv^{-1})	*0.0031/0.0056 (-45 %)*	*0.0042/0.0057 (-26 %)*	0.0041/0.0049 (-16 %)	0.0032/0.0033 (-3 %)
OC/ΔCO (μg m^{-3} ppbv^{-1})	*0.0093/0.0238 (-61 %)*	*0.0164/0.0276 (-41 %)*	0.0225/0.0287 (-22 %)	*0.0127/0.0153 (-17 %)*
Sea-Salt$_{PM2.5}$/ΔCO (μg m^{-3} ppbv^{-1})	*0.263/0.403 (-35 %)*	*0.352/0.262 (34 %)*	0.284/0.298 (-5 %)	*0.331/0.255 (30 %)*
Dust$_{PM2.5}$/ΔCO (μg m^{-3} ppbv^{-1})	*0.015/0.033 (-55 %)*	*0.042/0.062 (-32 %)*	*0.087/0.053 (64 %)*	0.018/0.017 (6 %)
Wind$_{SF}$ (m s^{-1})	*8.5/7.1 (20 %)*	*8.4/5.9 (42 %)*	4.4/4.7 (-6 %)	*7.7/6.6 (17 %)*
APT$_{6h}$ (mm)	*0.1/0.0 (NaN)*	0.0/0.0 (NaN)	0.0/0.0 (NaN)	0.0/0.0 (NaN)
APT (mm)	*24.7/0.0 (NaN)*	*22.6/0.2 (11200 %)*	*24.1/0.0 (NaN)*	*25.0/0.2 (12400 %)*
	All			
V$_f$ /ΔCO × 10^4 (μm^3 μm^{-2} ppbv^{-1})	3.42/7.55 (-55 %)			
R$_{eff-f}$ (μm)	0.158/0.147 (7 %)			
R$_f$ (μm)	0.176/0.171 (3 %)			
σ_f	0.471/0.470 (0 %)			
V$_c$ /ΔCO × 10^4 (μm^3 μm^{-2} ppbv^{-1})	2.04/2.12 (-4 %)			
R$_{eff-c}$ (μm)	1.956/2.085 (-6 %)			
R$_c$ (μm)	2.503/2.562 (-2 %)			
σ_c	*0.684/0.647 (6 %)*			

479

480 *% $difference = \dfrac{X_{High-rain} - X_{Low-rain}}{X_{Low-rain}} \times 100$

With the normalization technique, $PM_{2.5}/\Delta CO$ exhibits lower values in the high APT category for each season as compared to low APT conditions (Fig. 6), with differences between medians being statistically significant in DJF and MAM based on p-value < 0.05 with a Wilcoxon rank-sum test (Table 2). The DJF season exhibits the greatest reduction of this ratio (by 53%) in high APT conditions (0.29 μg m^{-3} ppbv^{-1} versus 0.62 μg m^{-3} ppbv^{-1} based on median values; Table 2). Therefore, these results suggest that it is plausible that wet scavenging has a marked impact on surface $PM_{2.5}$ at a remote ocean site in the WNAO. This also helps support the speculation proposed by Aldhaif et al. (2021) that wet scavenging can reconcile why, in particular for DJF, the high density of trajectories coming from North America correlates with a reduction in fine particulate pollution arriving at Bermuda as compared to other seasons. It is noteworthy that the highest median value of $PM_{2.5}/\Delta CO$ was for the low APT category of DJF providing support for how that season has both greater influence of aerosol transport from North America (when the precipitation scavenging potential is reduced during low APT periods) and the greatest sensitivity to the effects of precipitation over the WNAO owing to the widest range in this ratio's value between high and low APT categories.
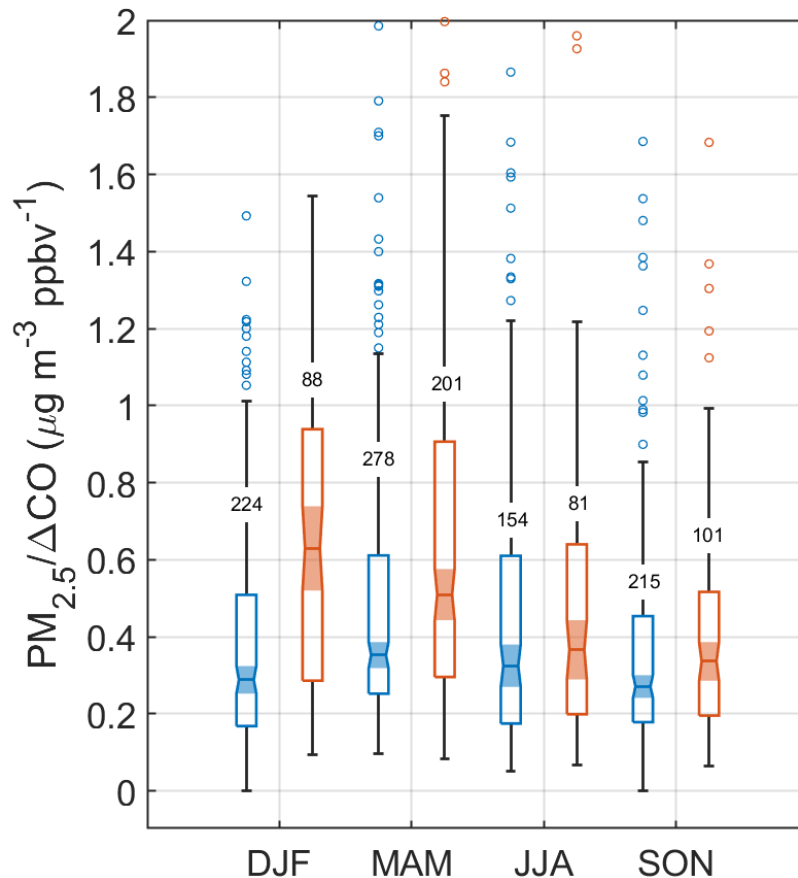
Figure 6. Box notch plot for each season comparing the $PM_{2.5}/\Delta CO$ ratio for Cluster 1 trajectories for high-APT (blue) and low-APT (orange) conditions. APT thresholds are based on 25th (< 0.9 mm) and 75th (> 13.5 mm) percentiles of APT for all trajectories reaching Bermuda between 1 January 2015 and 31 December 2019. The number of samples in each group is placed on whiskers.

Figure 7 additionally shows the seasonal sensitivity of PM$_{2.5}$/ΔCO to APT based on four bins of APT (bin ranges shown in Table S3) chosen in such a way to provide similar numbers of data points per bin for each particular season. We note that the general trends are preserved using similar bin ranges in each of the seasons. DJF and MAM show the greatest reductions from the first to last bin as expected based on Table 2, but these also were the only two seasons showing reductions between each successive bin. In contrast, SON and JJA exhibited more variable behavior with PM$_{2.5}$/ΔCO actually increasing between a pair of bins in each season. A number of reasons can potentially explain the less pronounced reduction in PM$_{2.5}$/ΔCO for SON and JJA: (i) lower values to begin with in the lowest APT bins (and thus lower potential for scavenging to occur); (ii) potential humidity effects associated with air masses at higher APT values promoting secondary aerosol formation (Huang et al., 2014; Quan et al., 2015; Ding et al., 2021); (iii) more influence from natural emissions in the form of dust (especially JJA) and sea salt (especially SON) (Aldhaif et al., 2021). Another noteworthy result is that the season with the clearest scavenging signature (DJF) shows the most sensitivity (i.e., steepest downward slope) between the first two APT bins (0.9 mm versus 4.3 mm) as there was a 26% reduction in PM$_{2.5}$/ΔCO (0.584 µg m^{-3} ppbv^{-1} to 0.435 µg m^{-3} ppbv^{-1}), resulting in a slope (units of µg m^{-3} ppbv^{-1} mm^{-1}) of -0.044 in contrast to slopes of -0.007 and -0.006 for the subsequent two pairs of bins in DJF. Tunved et al. (2013) also reported a similar exponential trend between particle mass and accumulated precipitation where an initial rapid decrease in particle mass was followed by a decreased removal rate of aerosol due to precipitation.
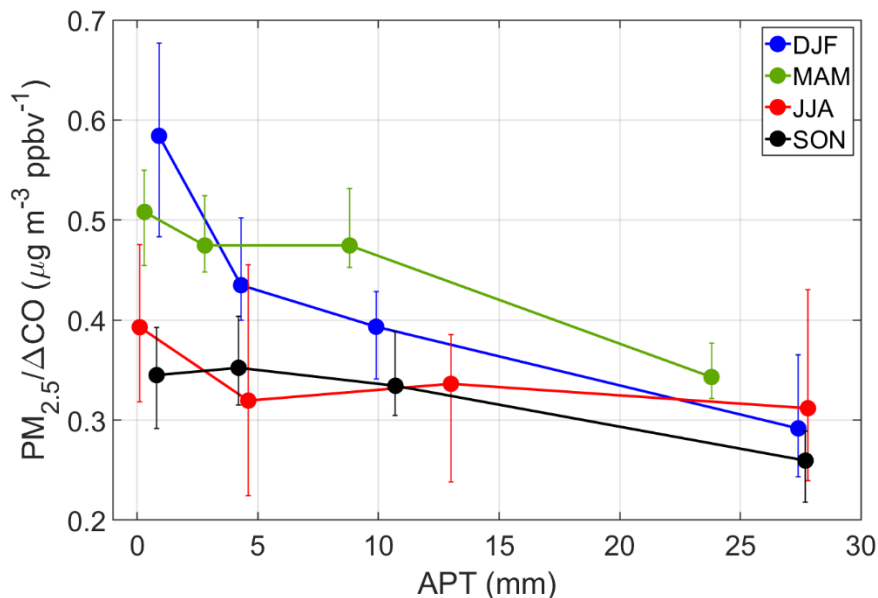
Figure 7. Seasonal sensitivity of PM$_{2.5}$/ΔCO to APT for Cluster 1 trajectories, divided based on four APT bins that have a similar number of data points per season. Markers denote median values and error bars represent the 95% confidence interval for medians based on a bootstrapping method (n = 100,000). Number of points per marker: DJF = 192 – 194; MAM = 247 – 251; JJA = 107 – 110; SON = 183 – 191.

We next address some additional details motivated by values shown in Table 2. We examine three aerosol constituents linked to anthropogenic outflow from North America, including sulfate, black carbon (BC), and organic carbon (OC) from MERRA-2 reanalysis. We recognize

534 that sulfate and OC have non-anthropogenic precursor vapors such as ocean-emitted dimethyl
535 sulfide and biogenic volatile organic compounds, respectively. Being the most abundant of the
536 three, sulfate exhibits the same characteristics as $PM_{2.5}$ when normalized by ΔCO with the sharpest
537 reduction at high APT conditions in DJF, followed by MAM, and then finally by JJA and SON
538 albeit with p-values > 0.05 for the latter two seasons as compared to low APT conditions. BC/ΔCO
539 ratios show the same relative characteristics between APT categories as sulfate/ΔCO for each
540 season, and mostly the same for OC/ΔCO except that the reduction in the median value in high
541 APT conditions for SON was significant (p-value < 0.05). Regardless of season, but most
542 pronounced in DJF, was the consistent result that OC/ΔCO exhibited the highest relative reduction
543 at high APT conditions (versus low APT) compared to BC and sulfate. Further work with more
544 expansive observational data is needed to better understand how different species respond to wet
545 scavenging.
546   Normalization by ΔCO was important for assessing transport efficiency of anthropogenic
547 pollution, but we also considered dust and sea salt without ΔCO normalization as they are
548 predominantly emitted by natural sources. Although outside the scope of this study, we caution
549 that MERRA-2 concentrations of sea salt in the $PM_{2.5}$ fraction may exceed those of total $PM_{2.5}$ as
550 measured at Ft. Prospect (Table 2) owing to the inherent differences in the two respective datasets
551 including the larger spatial scale covered by MERRA-2 as compared to the point measurements at
552 Ft. Prospect. Previous analysis of precipitation scavenging ratios over Bermuda showed that larger
553 aerosol types (e.g., sea salt) are removed more efficiently than smaller aerosol types (e.g., sulfate,
554 nitrate) (Galloway et al., 1993). Total sea salt and sea salt in the $PM_{2.5}$ fraction exhibited higher
555 median concentrations for the high APT category (p-value < 0.05) for all seasons except JJA,
556 which had more comparable values. This can be explained by how days experiencing high APT
557 exhibited significantly higher surface wind speeds around Bermuda for all seasons except JJA, for
558 which wind speeds in general were depressed. Therefore, the reduction of the $PM_{2.5}$/ΔCO ratio in
559 high APT conditions may actually be an underestimate of wet scavenging of North American
560 pollution outflow since local sea salt is higher windier days marked by high APT.
561   To put this last assertion on firmer ground, we examined local rain values as they could be
562 influential in terms of scavenging the locally generated sea salt. The median values of local rain
563 on high APT days for each season based on APT for the most recent 6 hours of trajectories arriving
564 at Bermuda (APT_{6h}) were $0.0 – 0.1$ mm, while median values of APT_{6h} on low APT days were 0
565 mm in each season. The only significant difference in median APT_{6h} values was in DJF when it
566 was 0.1 mm on high APT days in contrast to 0.0 mm on low APT days. Therefore, for DJF the
567 slightly enhanced APT_{6h} can possibly offset the greater sea salt emissions in terms of impacting
568 $PM_{2.5}$ levels over Bermuda. Results for the other major natural aerosol type (dust) reveal much
569 lower overall concentrations as compared to sea salt for both bulk sizes and the $PM_{2.5}$ fraction.
570 There was no consistent trend across the four seasons in terms of dust levels being higher for either
571 the low or high APT category, which is not unexpected as dust is not a major aerosol type expected
572 from North American outflow (Yu et al., 2020; Corral et al., 2021).
573
574 **3.3.1 Volume Size Distributions**
575   We next examine AERONET volume size distribution (VSD) relationships with APT. We
576 normalize the volume concentration data by corresponding ΔCO in the same way as was done for
577 $PM_{2.5}$, with the same condition of using data only when $\Delta CO > 3.2$ ppbv. A few cautionary details
578 are first noted about these data in comparison to APT: (i) there are limited VSD data in the
579 AERONET dataset, which is why we use all seasons of data together for Fig. 8 and Table 2; (ii)

18

AERONET data are representative of ambient conditions and changes in relative humidity can influence VSD profiles; and (iii) AERONET data are column-based and not necessarily representative of only the surface layer where the trajectories end in our analysis of HYSPLIT data. Related to the last point, past work noted that column optical properties over Bermuda can be weakly correlated with such measurements at the surface (Aryal et al., 2014) due largely to aerosol layers aloft (Ennis and Sievering, 1990). At the same time, studies have shown that there can be enhanced number and volume concentrations in the marine boundary layer versus the free troposphere over Bermuda (Horvath et al., 1990; Kim et al., 1990).

The median VSDs for both APT categories exhibit a bimodal profile with a more dominant coarse mode, consistent with what is already known for Bermuda based on AERONET data (Aldhaif et al., 2021). The unique aspect of this work is that in high APT conditions, there is a reduction in median volume concentration in the smaller mode between radii of 0.05 and ~1 μm, with a slight enhancement on the leading shoulder of the larger mode between radii of 1.71 and 2.94 μm (Fig. 8). The greatest relative reductions in the fine mode, which is more indicative of transported continental pollution, occurred between midpoint radii of 0.15 and 0.33 μm with relative reductions in those four bins (i.e., midpoint radii = 0.15, 0.19, 0.26, and 0.33 μm) ranging from 38% to 52%. The coarse mode peaked at larger radii (3.86 μm) in low APT conditions relative to high APT conditions (2.94 μm).

Table 2 reports VSD parameter values for the APT categories separated by fine and coarse modes. Although only significantly different based on 90% confidence (p-value = 0.09), the fine mode volume concentration normalized by ΔCO in the high APT category was less than half (45%) the value in the low APT category. There were insignificant differences between effective radii and volume median radii, in addition to the geometric standard deviation for the fine mode between APT categories. For the coarse mode, only the geometric standard deviation exhibited a significant difference by being higher in the high APT category (0.684 versus 0.647), although we presume that has less to do with actual scavenging effects and more to do with different times of the year where the relative abundance of different coarse particle type changes.
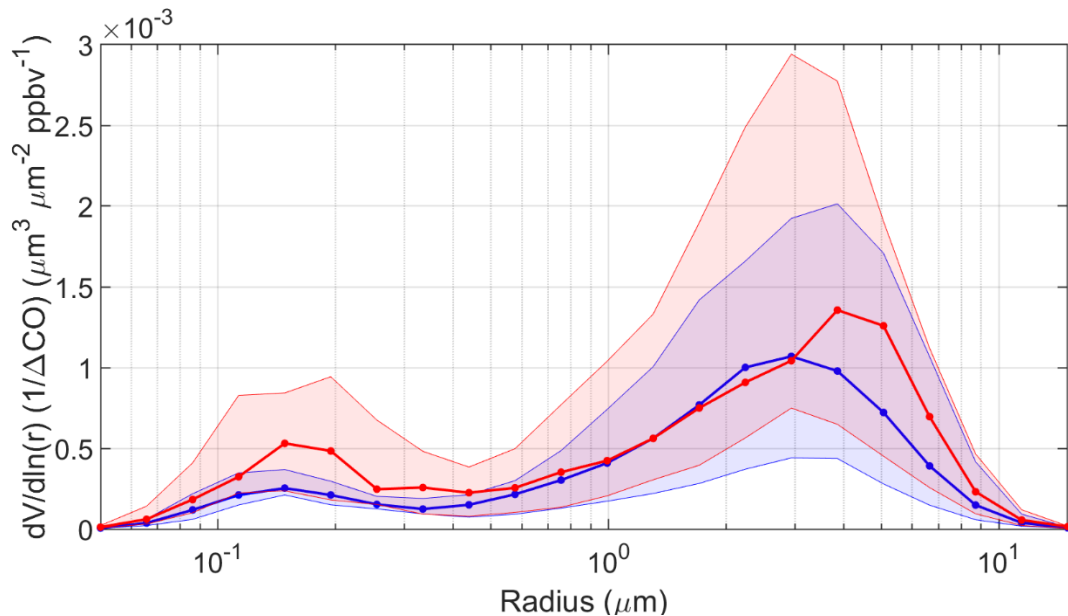

Figure 8. Volume size distributions (VSD) normalized by ΔCO for high APT (> 13 mm; blue, n = 16) and low APT (< 0.9 mm; red, n = 19) groups for Cluster 1 trajectories. Thick curves

correspond to medians and shaded areas extend to the 25th and 75th percentiles. VSDs are based on AERONET data between 1 January 2015 and 31 December 2019.

The AERONET results support the idea that scavenging on high APT days efficiently removes fine particulate matter but that there can still be appreciable levels of locally generated sea salt due to higher local surface winds on high APT days. Related to the columnar nature of AERONET data, it is important to note that others have reported large-scale subsidence of pollution from the mid and upper troposphere, especially in spring, based on enhanced ozone mixing ratios at the surface of Bermuda (Oltmans and Levy, 1992; Cooper et al., 1998; Milne et al., 2000; Li et al., 2002). Moreover, this phenomenon is synoptically favorable with the transport of North American polluted air behind cold fronts especially in spring (Moody et al., 1995) and often linked to the lifting of polluted air out of the boundary layer by convection over the continental U.S. (Prados et al., 1999). It is unclear based on the current dataset how effective these events were in impacting either the surface layer or columnar-based aerosol measurements at Bermuda.

3.4 GEOS-Chem Model Results

We conduct four GEOS-Chem simulations of the ^{210}Pb submicron aerosol tracer including a) one standard simulation; b) same as the standard simulation but with the ^{222}Rn tracer emissions from the North American continent (25-60°N, 130-70°W) removed; c) same as the standard simulation but without ^{210}Pb scavenging due to large-scale precipitation; and d) same as the standard simulation but without ^{210}Pb scavenging by convective precipitation. The difference between a) and b) quantifies the North American contribution to atmospheric ^{210}Pb concentrations. The difference between a) and c) reflects the role of large-scale precipitation scavenging, while the difference between a) and d) reflects that of convective precipitation scavenging in determining atmospheric ^{210}Pb concentrations. All model simulations are conducted for the period from September 2016 to December 2017 with the first four months for spin-up. Monthly mean outputs for 2017 are used for analysis, which is a representative year within the time frame of the analysis presented in Sections 3.1-3.3. This is confirmed by the seasonal APT box chart constructed in Fig. S6 using only 2017 data, which nearly follows the trend observed when the five-year data are used (Fig. 5).
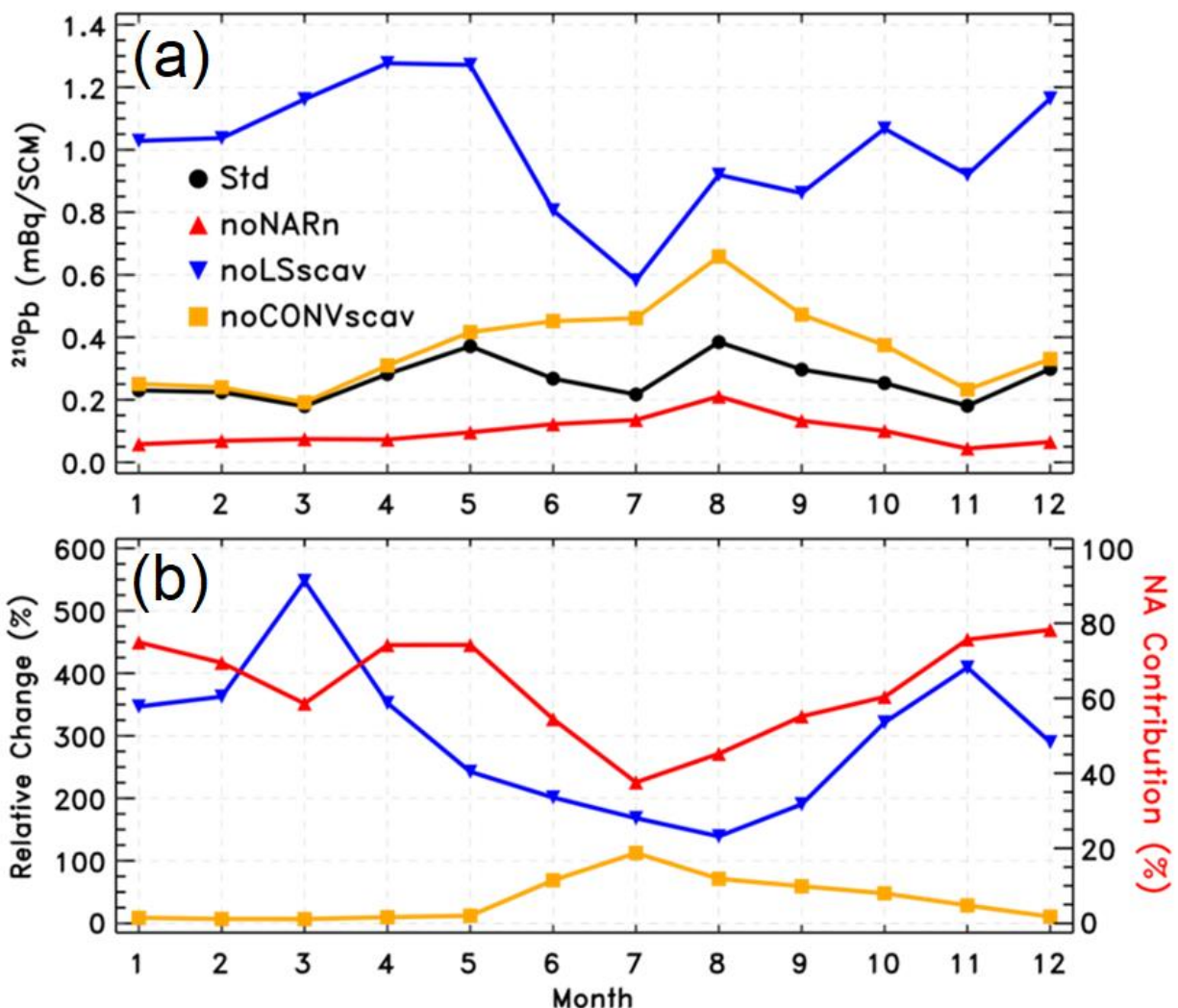
Figure 9. Simulated monthly surface ^{210}Pb tracer concentrations submicron mBq/SCM at Bermuda (32.31° N, 64.75° W) in 2017 as a way to assess effects of precipitation scavenging on North American outflow. Panel (a): monthly mean surface ^{210}Pb concentrations in the standard simulation ("Std") and three sensitivity simulations, i.e., without North American ^{222}Rn emissions ("noNARn"), without large-scale precipitation scavenging ("noLSscav"), and without convective precipitation scavenging ("noCONVscav"). Panel (b): percentage changes, i.e., (noLSscav-Std)/Std×100 in blue and (noCONVscav-Std)/Std×100 in orange, and the North American contribution in red, i.e., (Std–noNARn)/Std×100.

Figure 9a shows monthly mean surface ^{210}Pb concentrations at Bermuda for 2017 in the standard simulation and three sensitivity simulations. Figure 9b plots the relative changes in simulated ^{210}Pb concentrations due to the effects of large-scale or convective precipitation scavenging. Also included in Fig. 9b is the North American contribution. The standard model simulates a seasonality in ^{210}Pb concentrations with two distinct peaks in May and August (upper panel). The May peak is a result of increased transport from North America in combination with reduced scavenging. In contrast, the August peak results from long-range transport from other continents (e.g., North Africa, Europe) along the southern edge of the Bermuda High. The lows in

21

659 March and November are attributed to strong large-scale precipitation scavenging, and the low in
660 July is associated with enhanced convective precipitation scavenging. The sensitivity simulations
661 clearly show that the role of large-scale precipitation scavenging in affecting surface [210]Pb
662 concentrations at Bermuda is much larger in winter/spring than in summer, with a maximum in
663 March (lower panel), while convective scavenging also plays an important role in summer. The
664 relative contribution of North American [222]Rn emissions is largest in winter (~75-80%), suggesting
665 air masses reaching Bermuda often experience large-scale precipitation scavenging while
666 traveling from the North American continent during winter. While the model may have limitations
667 and inherent uncertainties, its results are at least consistent with results shown already, putting our
668 conclusions on firmer ground.
669
670 **3.5 Airborne Case Study**
671   The DJF season has been shown in this study to exhibit the greatest potential for wet
672 scavenging and the highest density of trajectories from North America reaching Bermuda. To
673 probe deeper now, we take advantage of data from ACTIVATE RF6 on 22 February 2020, which
674 characterized the intermediate region between North America and Bermuda. Weather in the
675 ACTIVATE domain on this day was characterized by a transition from post-cold front conditions
676 to high pressure. A cold front passed over Bermuda the previous day at approximately 18:00 UTC
677 on 21 February, and by the flight period of RF06 was approximately 600 km southeast of the
678 island. Meanwhile, a broad but weakening area of surface high pressure continued eastward into
679 the southeast U. S. Winds in the boundary layer were southwesterly at around 5 m s^{-1} near the base
680 of operations (NASA Langley Research Center; Hampton, Virginia), which were associated with
681 a weak trough on the northeast side of the high pressure system. These winds shifted to north-
682 northwest near the coast at 2.5 m s^{-1} and north-northeast at 7.4 m s^{-1} near the far end of the flight
683 track; Bermuda reported north-northeast winds around 9 m s^{-1} during this period. Aloft, 500 hPa
684 flow was from the west-northwest. NASA Langley reported few to no clouds during the flight
685 period, while Bermuda reported broken clouds with multiple layers (with bases around 900 m and
686 1800 m) and rain showers at or near the airport. This is consistent with satellite imagery (Fig. 10a),
687 which shows an area of scattered to broken cumulus and stratocumulus extending from the cold
688 front near Bermuda to the edge of the Gulf Stream off the U.S. East Coast. Satellite-retrieved cloud
689 bases were at 1–2 km, with cloud tops ranging from 1.5–3.5 km; from the HU-25 Falcon flight
690 legs, cloud bases encountered along the flight track were 750–1100 m and cloud tops were 1200–
691 1800 m.
692
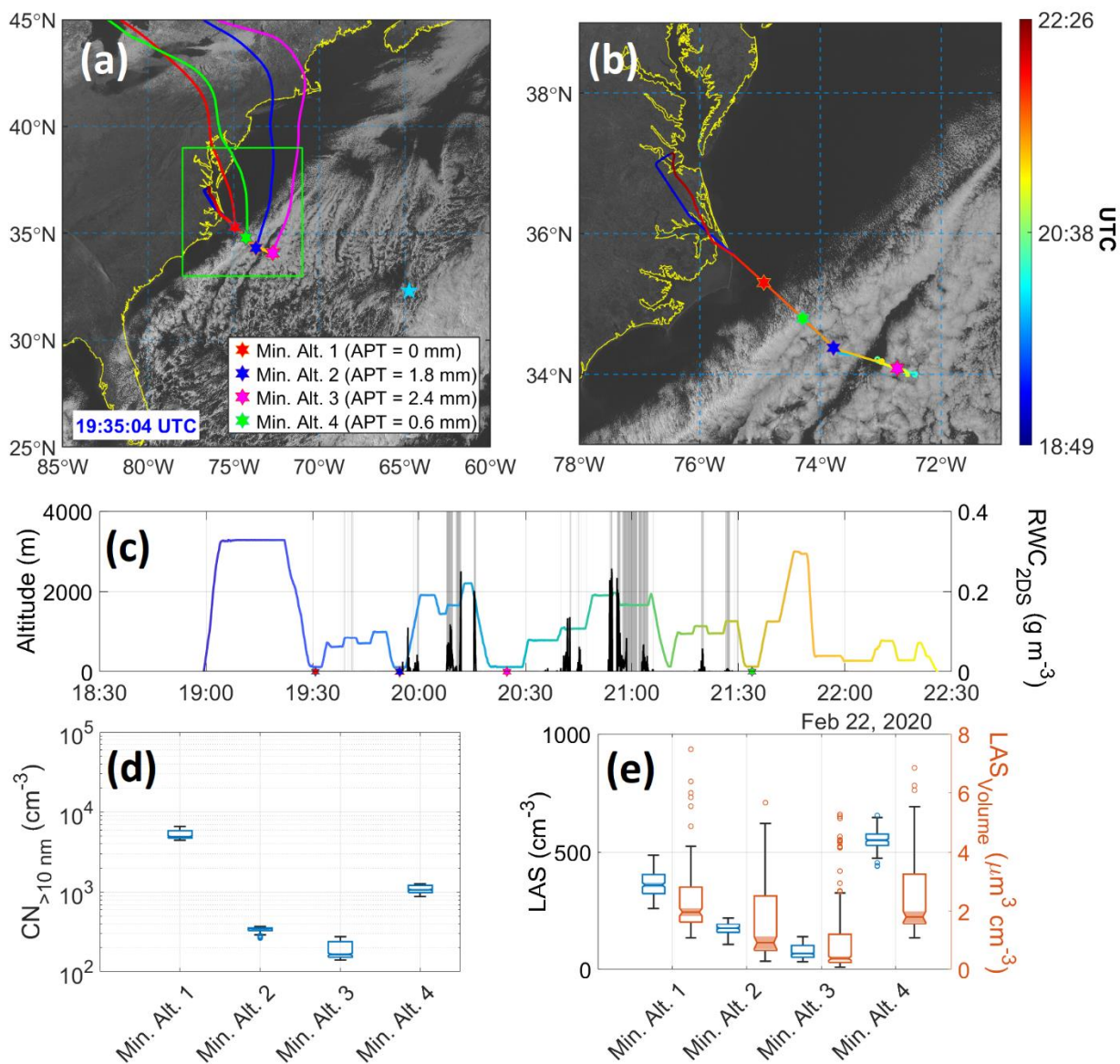
Figure 10. Summary of ACTIVATE's Research Flight 6 on 22 February 2020. (a) HU-25 Falcon flight track overlaid on GOES-16 imagery of the WNAO (Bermuda denoted by blue star) also showing 96 hour back-trajectories calculated for each respective Min Alt. leg. The midpoint of the four Min. Alt. legs are marked including values for the accumulated precipitation along the trajectory (APT) for the recent history of the sampled air masses when they were over the ocean (time over land excluded from APT calculation). (b) Zoomed in version of panel (a) focused on the flight path. (c) Time series of Falcon altitude colored by flight UTC time (color bar in panel b) and rain water content (RWC) from the 2DS probe. Gray shaded bars signify when FCDP liquid water content exceeded 0.05 g m^{-3}, indicative of cloud legs. The same four colored stars from (a) are shown on the x-axis to indicate where they occurred. (d-e) Box notch plots of the leg-mean Min. Alt. values of CPC particle concentration (> 0.01 μm), and the number and volume concentrations of the LAS (> 0.09 μm).

707   Figure 10a shows the general flight path, which involved flying to a point southeast of the
708 operations base (Hampton, Virginia) and then re-tracing the path back to land. Four HYSPLIT
709 back-trajectories are shown (Fig. 10a) corresponding to midpoints of each Min. Alt. leg when the
710 aircraft was at its lowest altitude (~500 ft). APT calculations were conducted for segments of those
711 four trajectories that were over the ocean to focus on wet removal clouds over the WNAO.
712 Negligible rain accumulated up to the point of the Min. Alt. 1 leg, as there were cloud-free
713 conditions between land and that offshore point. In contrast, the next three Min. Alt. legs show
714 higher APT values ranging from 0.6 to 2.4 mm, consistent with the GOES-16 imagery showing
715 cloud fraction increasing just to the southeast of the Min. Alt. 1 leg. Expectedly, APT values
716 progressively increased with offshore distance as a result of air masses being exposed to clouds
717 for longer periods. Figure S7 shows 27 trajectories obtained for each Min. Alt. leg based on
718 ensemble trajectory analysis which is a technique available in HYSPLIT to evaluate uncertainties
719 in trajectory calculations by offsetting the meteorological data by a fixed grid factor. Average APT
720 values based on ensemble analysis (Fig. S7) were 0.29, 1.18, 2.27, and 0.73 mm corresponding to
721 Min. Alt. 1, 2, 3, and 4 legs, respectively, which follow the trend observed in Fig. 10.
722   Shortly after the Min. Alt. 1 leg, the Falcon conducted two consecutive pairs of BCB and
723 ACB legs (i.e., below cloud base followed by above cloud base), followed by a slant descent to
724 the Min. Alt. 2 leg, where RWC values were enhanced (up to 0.02 g m^{-3} at 19:55:22 UTC) owing
725 to precipitation from overlying clouds. Very shortly thereafter, RWC reached as high as 0.11 g m^{-3}
726 (19:56:50 UTC) in the slant ascent profile passing through clouds. The APT value in Min. Alt. 2
727 leg was 1.8 mm. A significant reduction was observed in the aerosol number and volume
728 concentrations for the Min. Alt. 2 leg as compared to the Min. Alt. 1 leg (Figs. 10d-e). Table S4
729 reports the statistics for aerosol parameters measured in Min. Alt. legs (Fig. 10). CPC (> 10 nm)
730 concentrations dropped by 93% from a leg-median value of 4938 cm^{-3} during Min. Alt. 1 to 345
731 cm^{-3} during Min. Alt. 2, whereas the LAS number and volume (> 100 nm) concentrations dropped
732 from 360 cm^{-3} to 174 cm^{-3} and from 2.0 µm^3 cm^{-3} to 0.9 µm^3 cm^{-3}, respectively. Size distribution
733 data in those two legs show a significant reduction in particle concentration across the full diameter
734 range as measured by the SMPS and LAS (Fig. 11). A notable feature from the SMPS was a
735 pronounced peak between 3.5 – 14.1 nm suggestive of nucleation, that was absent in subsequent
736 Min. Alt. legs, presumably owing to some combination of coagulation and scavenging.

24
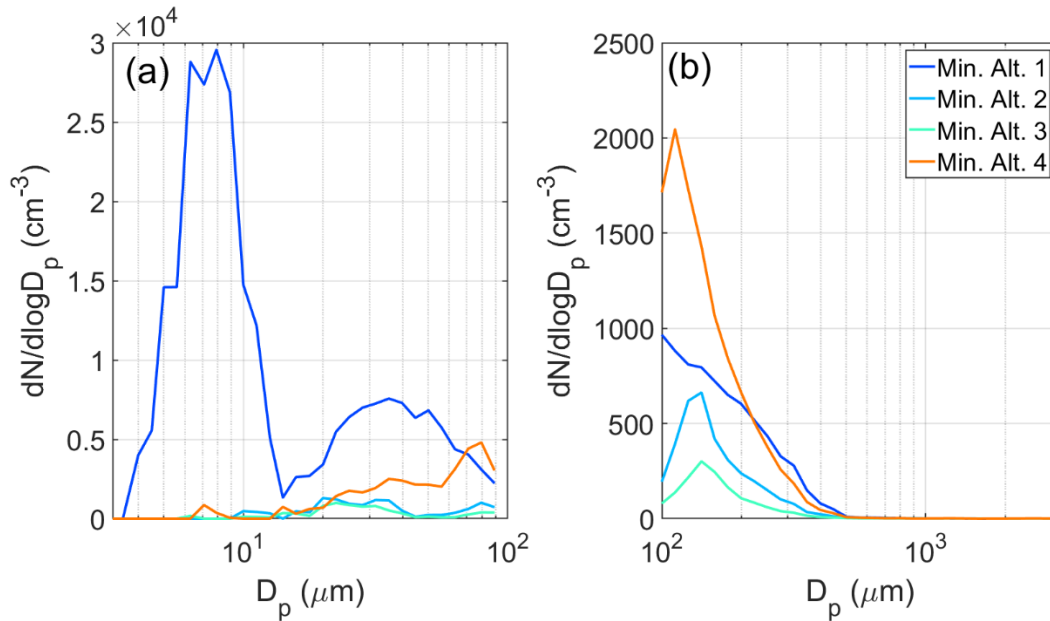
Figure 11. Aerosol size distribution comparison (a = SMPS, b = LAS) between the four HU-25 Falcon Min. Alt. legs during ACTIVATE Research Flight 6, as shown in Fig. 10.

The aircraft continued southeast after the Min. Alt. 2 leg and passed through more patches of precipitation, leading to the highest APT value of 2.4 mm in the Min. Alt. 3 leg, where leg-median values were as follows: CPC = 165 cm^{-3}, LAS number = 66 cm^{-3}, LAS volume = 0.4 µm^3 cm^{-3}. While the SMPS distributions in the Min. Alt. 2 and 3 legs were very similar, the LAS size distribution in the Min. Alt. 3 leg is shifted towards lower concentrations, especially below 400 nm. On the path back towards Virginia, the Falcon conducted one final Min. Alt. 4 leg right before the boundary between cloudy and clear air, with the APT value being 0.6 mm. Between the Min. Alt. 3 and 4 legs, again, significant RWC values were observed reaching as high as 0.26 g m^{-3} at 20:54:20 UTC. Aerosol concentration measurements increased relative to the Min. Alt. 2 and 3 legs (leg-median values): CPC = 1076 cm^{-3}, LAS number = 545 cm^{-3}, LAS volume = 1.8 µm^3 cm^{-3}. It is difficult to compare results from the Min. Alt. 1 and 4 legs as ~2 hours had passed and there were different conditions impacting the two respective sampled air masses. The size distributions varied considerably for the Min. Alt. 4 leg as compared to the other three legs with increased concentrations between 20-200 nm, presumably as a result of continued pollution outflow and more photochemistry and aerosol growth processing as compared to earlier in the day.

To conclude, it is plausible based on the case flight data that the emerging presence of clouds and precipitation led to the substantial reduction of aerosol particles with distance offshore via wet scavenging processes. Further research is warranted with more extensive data to move closer to showing causal relationships between precipitation and aerosol particles. For instance, a few points of caution from RF6 are worth mentioning. First, the coastal trajectories in Fig. 10 corresponding to the different Min Alt. legs originated from varying places extending from the Virginia coast up north towards Cape Cod, Massachusetts. Secondly, cloud dynamics and boundary layer structure can vary offshore. Related to the latter, PBLH data obtained from MERRA-2 along the flight track revealed that there were deeper boundary layers farther offshore, but not sufficiently deeper to fully explain the reductions in aerosol concentration: PBLH

25

766 corresponding to Min. Alt. 1/2/3/4 = 1156/1728/1740/1530 m. Lastly, aerosol concentrations
767 linked to continental outflow naturally decrease anyways offshore, including in cloud-free
768 conditions, owing to dilution during transport.
769
770 **4. Conclusion**

771   This study examines the sensitivity of surface aerosol characteristics over a remote area of
772 the western North Atlantic Ocean (Bermuda) to precipitation along trajectories coming from North
773 America. Based on trajectory clustering with HYSPLIT data, two characteristic transport corridors
774 to Bermuda's surface layer (100 m AGL) were identified, with the focus being the one coming
775 from North America (Cluster 1). Seasonal analysis of HYSPLIT and Bermuda surface data showed
776 that JJA is distinct in terms of having transport from the southeast with the other seasons, especially
777 DJF, having more North American influence with higher concentrations of CO. Comparing Cluster
778 1 trajectories data between high (>13.5 mm) and low (<0.9 mm) accumulated precipitation along
779 trajectories (APT), there was a clear signature of wet scavenging effects by precipitation with more
780 than a two-fold reduction in $PM_{2.5}/\Delta CO$ in DJF (0.29 µg m^{-3} ppbv^{-1} versus 0.62 µg m^{-3} ppbv^{-1}),
781 with the reduction being less severe for other seasons. The greatest sensitivity of $PM_{2.5}/\Delta CO$ to
782 APT was at the lowest values (up to ~5 mm; slope of -0.044 µg m^{-3} ppbv^{-1} mm^{-1}), above which
783 the descending slope of $PM_{2.5}/\Delta CO$ versus APT was less steep.
784   Speciated data indicate that anthropogenic species such as sulfate, black carbon, and
785 organic carbon are reduced as a function of APT (much like $PM_{2.5}$). However, sea salt was not
786 necessarily reduced and at times could even be higher at Bermuda with high APT conditions,
787 which is attributed to higher local wind speeds. Analysis of AERONET volume size distribution
788 data at Bermuda confirms the substantial reduction of fine mode volume concentrations in contrast
789 to a smaller change in the coarse mode on high APT days. GEOS-Chem simulations of the
790 radionuclide aerosol tracer ^{210}Pb confirm that North American influence at the surface of Bermuda
791 is highest in DJF, with those air masses significantly impacted by large-scale (i.e., stratiform and
792 anvil) precipitation scavenging; furthermore, convective scavenging is shown to play an important
793 role in summer months. A research flight from ACTIVATE on 22 February 2020 demonstrates a
794 significant gradient in aerosol number and volume concentrations offshore of North America as
795 soon as trajectories start passing across clouds, consistent with increasing APT away from the
796 coast leading to increased aerosol particle removal.
797   Our results have implications for other remote marine regions impacted by transport of
798 continental emissions. These results also highlight the important role of precipitation in modifying
799 aerosol levels, including potentially their vertical distribution (e.g., Luan and Jaeglé, 2013), along
800 continental outflow trajectories. We show that cloud and precipitation processes along trajectories
801 have significant impacts on resultant aerosol characteristics. Therefore, it is important to strongly
802 constrain we scavenging processes in models to improve aerosol forecasting over the WNAO
803
804
805

822   *Author contributions.* HD and MA conducted the analysis. AS and HD prepared the manuscript.
823   HL and BZ performed GEOS-Chem model radionuclide simulations and output analysis. All
824   authors contributed by providing input and/or participating in airborne data collection.

825   *Competing interests.* The authors declare that they have no conflict of interest.

ACMAP and MAP programs. GEOS-Chem input files were obtained from the GEOS-Chem Data Portal enabled by Compute Canada.

References

Aldhaif, A. M., Lopez, D. H., Dadashazar, H., Painemal, D., Peters, A. J., and Sorooshian, A.: An Aerosol Climatology and Implications for Clouds at a Remote Marine Site: Case Study Over Bermuda, Journal of Geophysical Research: Atmospheres, 126, e2020JD034038, https://doi.org/10.1029/2020JD034038, 2021.

Altieri, K. E., Hastings, M. G., Gobel, A. R., Peters, A. J., and Sigman, D. M.: Isotopic composition of rainwater nitrate at Bermuda: The influence of air mass source and chemistry in the marine boundary layer, J Geophys Res-Atmos, 118, 11, 304–11, 316, https://doi.org/10.1002/jgrd.50829, 2013.

Anderson, J. R., Buseck, P. R., Patterson, T. L., and Arimoto, R.: Characterization of the Bermuda tropospheric aerosol by combined individual-particle and bulk-aerosol analysis, Atmos Environ, 30, 319-338, https://doi.org/10.1016/1352-2310(95)00170-4, 1996.

Arimoto, R., Duce, R. A., Savoie, D. L., and Prospero, J. M.: Trace-Elements in Aerosol-Particles from Bermuda and Barbados - Concentrations, Sources and Relationships to Aerosol Sulfate, J Atmos Chem, 14, 439-457, https://doi.org/10.1007/BF00115250,1992.

Arimoto, R., Duce, R. A., Ray, B. J., Ellis, W. G., Cullen, J. D., and Merrill, J. T.: Trace-Elements in the Atmosphere over the North-Atlantic, J Geophys Res-Atmos, 100, 1199-1213, https://doi.org/10.1029/94jd02618, 1995.

Arimoto, R., Snow, J. A., Graustein, W. C., Moody, J. L., Ray, B. J., Duce, R. A., Turekian, K. K., and Maring, H. B.: Influences of atmospheric transport pathways on radionuclide activities in aerosol particles from over the North Atlantic, J Geophys Res-Atmos, 104, 21301-21316, https://doi.org/10.1029/1999JD900356, 1999.

Arimoto, R.: Eolian Dust and Climate: Relationships to Sources, Tropospheric Chemistry, Transport and Deposition. Earth-Science Reviews, 54(1), 29-42, https://doi.org/10.1016/S0012-8252(01)00040-X, 2001.

Aryal, R. P., Voss, K. J., Terman, P. A., Keene, W. C., Moody, J. L., Welton, E. J., and Holben, B. N.: Comparison of surface and column measurements of aerosol scattering properties over the western North Atlantic Ocean at Bermuda, Atmos Chem Phys, 14, 7617-7629, https://doi.org/10.5194/acp-14-7617-2014, 2014.

Bey, I., Jacob, D. J., Yantosca, R. M., Logan, J. A., Field, B. D., Fiore, A. M., Li, Q. B., Liu, H., Mickley, L. J. and Schultz, M. G.: Global modeling of tropospheric chemistry with assimilated meteorology: Model description and evaluation, J. Geophys. Res. Atmos., 106(D19), 23073–23095, https://doi.org/10.1029/2001JD000807, 2001.

Brattich, E., Liu, H., Tositti, L., Considine, D. B., and Crawford, J. H.: Processes controlling the seasonal variations in 210Pb and 7Be at the Mt. Cimone WMO-GAW global station, Italy: a

879   model analysis, Atmos. Chem. Phys., 17(2), 1061-1080, https://doi.org/10.5194/acp-17-1061-
880   2017, 2017.

881   Cabello, M., Orza, J.A.G., Galiano, V., Ruiz, G.: Influence of meteorological input data on
882   backtrajectory cluster analysis – a seven-year study for southeastern Spain. Advances in Science
883   and Research 2, 65–70, https://doi.org/10.5194/asr-2-65-2008, 2008.

884   Chen, L. Q., and Duce, R. A.: The Sources of Sulfate, Vanadium and Mineral Matter in Aerosol-
885   Particles over Bermuda, Atmos Environ, 17, 2055-2064, https://doi.org/10.1016/0004-
886   6981(83)90362-1, 1983.

887   Cooper, O. R., Moody, J. L., Davenport, J. C., Oltmans, S. J., Johnson, B. J., Chen, X., Shepson,
888   P. B., and Merrill, J. T.: Influence of springtime weather systems on vertical ozone distributions
889   over three North American sites, J Geophys Res-Atmos, 103, 22001-22013,
890   https://doi.org/10.1029/98JD01801, 1998.

891   Corral, A. F., Braun, R. A., Cairns, B., Gorooh, V. A., Liu, H., Ma, L., Mardi, A. H., Painemal,
892   D., Stamnes, S., van Diedenhoven, B., Wang, H., Yang, Y., Zhang, B., and Sorooshian, A.: An
893   Overview of Atmospheric Features Over the Western North Atlantic Ocean and North American
894   East Coast – Part 1: Analysis of Aerosols, Gases, and Wet Deposition Chemistry, Journal of
895   Geophysical Research: Atmospheres, 126, e2020JD032592,
896   https://doi.org/10.1029/2020JD032592, 2021.

897   Cutter, G. A.: Metalloids in Wet Deposition on Bermuda - Concentrations, Sources, and Fluxes,
898   J Geophys Res-Atmos, 98, 16777-16786, https://doi.org/10.1029/93JD01689, 1993.

899   Dadashazar, H., Painemal, D., Alipanah, M., Brunke, M., Chellappan, S., Corral, A. F., Crosbie,
900   E., Kirschler, S., Liu, H., Moore, R., Robinson, C., Scarino, A. J., Shook, M., Sinclair, K.,
901   Thornhill, K. L., Voigt, C., Wang, H., Winstead, E., Zeng, X., Ziemba, L., Zuidema, P., and
902   Sorooshian, A.: Cloud Drop Number Concentrations over the Western North Atlantic Ocean:
903   Seasonal Cycle, Aerosol Interrelationships, and Other Influential Factors, Atmos. Chem. Phys.
904   Discuss., 2021, 1-36, https://doi.org/10.5194/acp-2021-153, 2021.

905   Davis, R. E., Hayden, B. P., Gay, D. A., Phillips, W. L., and Jones, G. V.: The North Atlantic
906   Subtropical Anticyclone, J Climate, 10, 728-744, https://doi.org/10.1175/1520-
907   0442(1997)010<0728:tnasa>2.0.co;2, 1997.

908   Dimitriou, K., Remoundaki, E., Mantas, E., Kassomenos, P.: Spatial distribution of source areas
909   of $PM_{2.5}$ by Concentration Weighted Trajectory (CWT) model applied in PM2.5 concentration
910   and composition data, Atmospheric Environment 116, 138–145,
911   https://doi.org/10.1016/j.atmosenv.2015.06.021, 2015.

912   Ding, J., Dai, Q., Zhang, Y., Xu, J., Huangfu, Y., Feng, Y.: Air humidity affects secondary
913   aerosol formation in different pathways, Science of The Total Environment 759, 143540,
914   https://doi.org/10.1016/j.scitotenv.2020.143540, 2021.
915
916   Dubovik, O., Holben, B., Eck, T. F., Smirnov, A., Kaufman, Y. J., King, M. D., Tanré, D., and
917   Slutsker, I.: Variability of Absorption and Optical Properties of Key Aerosol Types Observed in

918   Worldwide Locations, J Atmos Sci, 59, 590-608, https://doi.org/10.1175/1520-
919   0469(2002)059<0590:VOAAOP>2.0.CO;2, 2002.

920   Eastham, S. D., Weisenstein, D. K. and Barrett, S. R. H.: Development and evaluation of the
921   unified tropospheric-stratospheric chemistry extension (UCX) for the global chemistry-transport
922   model GEOS-Chem, Atmos. Environ., 89, 52–63,
923   https://doi.org/10.1016/j.atmosenv.2014.02.001, 2014.

924   Engström, A., Magnusson, L.: Estimating trajectory uncertainties due to flow dependent errors in
925   the atmospheric analysis. Atmospheric Chemistry and Physics 9, 8857–8867,
926   https://doi.org/10.5194/acp-9-8857-2009, 2009.

927   Ennis, G., and Sievering, H.: Vertical Profile of Elemental Concentrations in Aerosol Particles in
928   the Bermuda Area during Gce/Case/Watox, Global Biogeochem Cy, 4, 179-188,
929   https://doi.org/10.1029/GB004i002p00179, 1990.

930   Galloway, J. N., Tokos, J. J., Knap, A. H., and Keene, W. C.: Local influences on the
931   composition of precipitation on Bermuda, Tellus B: Chemical and Physical Meteorology, 40,
932   178-188, https://doi.org/10.3402/tellusb.v40i3.15905, 1988.

933   Galloway, J. N., Keene, W. C., Artz, R. S., Miller, J. M., Church, T. M., and Knap, A. H.:
934   Processes controlling the concentrations of $SO(4)(=)$, $NO(3)(-)$, $NH(4)(+)$, $H(+)$, $HCOO(T)$ and
935    $CH(3)COO(T)$ in precipitation on Bermuda, Tellus B, 41, 427-443, 1989.

936   Galloway, J. N., Savoie, D. L., Keene, W. C., and Prospero, J. M.: The Temporal and Spatial
937   Variability of Scavenging Ratios for Nss Sulfate, Nitrate, Methanesulfonate and Sodium in the
938   Atmosphere over the North-Atlantic Ocean, Atmos Environ a-Gen, 27, 235-250,
939   https://doi.org/10.1016/0960-1686(93)90354-2, 1993.

940   Garrett, T., Zhao, C., Novelli, P.: Assessing the relative contributions of transport efficiency and
941   scavenging to seasonal variability in Arctic aerosol. Tellus B: Chemical and Physical
942   Meteorology 62, 190–196, https://doi.org/10.1111/j.1600-0889.2010.00453.x, 2010.

943   Gebhart, K.A., Schichtel, B.A., Barna, M.G.: Directional Biases in Back Trajectories Caused by
944   Model and Input Data. Journal of the Air & Waste Management Association, 55, 1649–1662,
945   https://doi.org/10.1080/10473289.2005.10464758, 2005.

946   Gelaro, R., McCarty, W., Suarez, M. J., Todling, R., Molod, A., Takacs, L., Randles, C. A., 886
947   Darmenov, A., Bosilovich, M. G., Reichle, R., Wargan, K., Coy, L., Cullather, R., Draper, C.,
948   Akella, S., Buchard, V., Conaty, A., da Silva, A. M., Gu, W., Kim, G. K., Koster, R., Lucchesi,
949   R., Merkova, D., Nielsen, J. E., Partyka, G., Pawson, S., Putman, W., Rienecker, M., Schubert,
950   S. D., Sienkiewicz, M., and Zhao, B.: The Modern-Era Retrospective Analysis for Research and
951   Applications, Version 2 (MERRA-2), J Climate, 30, 5419-5454, https://doi.org/10.1175/Jcli-D-
952   16-0758.1, 2017.

953   Giles, D. M., Sinyuk, A., Sorokin, M. G., Schafer, J. S., Smirnov, A., Slutsker, I., Eck, T. F.,
954   Holben, B. N., Lewis, J. R., Campbell, J. R., Welton, E. J., Korkin, S. V., and Lyapustin, A. I.:
955   Advancements in the Aerosol Robotic Network (AERONET) Version 3 database – automated

956   near-real-time quality control algorithm with improved cloud screening for Sun photometer
957   aerosol optical depth (AOD) measurements, Atmos. Meas. Tech., 12, 169-209,
958   https://doi.org/10.5194/amt-12-169-2019, 2019.

959   Govender, P. and Sivakumar, V.: Application of k-means and hierarchical clustering techniques
960   for analysis of air pollution: A review (1980–2019), Atmospheric Pollution Research, 11, 40–56,
961   https://doi.org/10.1016/j.apr.2019.09.009, 2020.

962   Government of Bermuda: 2016 Population and Housing Census Report. Retrieved from
963   https://www.gov.bm/articles/2016-population-and-housing-census-report, 2019.

964   Hilario, M. R. A., Cruz, M. T., Bañaga, P. A., Betito, G., Braun, R. A., Stahl, C., Cambaliza, M.
965   O., Lorenzo, G. R., MacDonald, A. B., AzadiAghdam, M., Pabroa, P. C., Yee, J. R., Simpas, J.
966   B., and Sorooshian, A.: Characterizing Weekly Cycles of Particulate Matter in a Coastal
967   Megacity: The Importance of a Seasonal, Size-Resolved, and Chemically Speciated Analysis,
968   Journal of Geophysical Research: Atmospheres, 125, e2020JD032614,
969   https://doi.org/10.1029/2020JD032614, 2020.

970   Hilario, M. R. A., Crosbie, E., Shook, M., Reid, J. S., Cambaliza, M. O. L., Simpas, J. B. B.,
971   Ziemba, L., DiGangi, J. P., Diskin, G. S., Nguyen, P., Turk, F. J., Winstead, E., Robinson, C. E.,
972   Wang, J., Zhang, J., Wang, Y., Yoon, S., Flynn, J., Alvarez, S. L., Behrangi, A., and Sorooshian,
973   A.: Measurement report: Long-range transport patterns into the tropical northwest Pacific during
974   the CAMP2Ex aircraft campaign: chemical composition, size distributions, and the impact of
975   convection, Atmos. Chem. Phys., 21, 3777-3802, https://doi.org/10.5194/acp-21-3777-2021,
976   2021.

977   Holben, B. N., Eck, T. F., Slutsker, I., Tanré, D., Buis, J. P., Setzer, A., Vermote, E., Reagan, J.
978   A., Kaufman, Y. J., Nakajima, T., Lavenu, F., Jankowiak, I., and Smirnov, A.: AERONET—A
979   Federated Instrument Network and Data Archive for Aerosol Characterization, Remote Sens
980   Environ, 66, 1-16, https://doi.org/10.1016/S0034-4257(98)00031-5, 1998.

981   Horvath, H., Gunter, R. L., and Wilkison, S. W.: Determination of the Coarse Mode of the
982   Atmospheric Aerosol Using Data from a Forward-Scattering Spectrometer Probe, Aerosol Sci
983   Tech, 12, 964-980, https://doi.org/10.1080/02786829008959407, 1990.

984   Hsu, Y.-K., Holsen, T.M., Hopke, P.K.: Comparison of hybrid receptor models to locate PCB
985   sources in Chicago. Atmospheric Environment 37, 545–562, https://doi.org/10.1016/s1352-
986   2310(02)00886-5, 2003.

987   Huang, S., Arimoto, R., Rahn, K.A.: Changes in atmospheric lead and other pollution elements
988   at Bermuda. Journal of Geophysical Research 101, 21033–21040, https://doi.org/
989   10.1029/96jd02001, 1996.

990   Huang, R.-J., Zhang, Y., Bozzetti, C., Ho, K.-F., Cao, J.-J., Han, Y., Daellenbach, K.R., Slowik,
991   J.G., Platt, S.M., Canonaco, F., Zotter, P., Wolf, R., Pieber, S.M., Bruns, E.A., Crippa, M.,
992   Ciarelli, G., Piazzalunga, A., Schwikowski, M., Abbaszade, G., Schnelle-Kreis, J., Zimmermann,
993   R., An, Z., Szidat, S., Baltensperger, U., Haddad, I.E., Prévôt, A.S.H.: High secondary aerosol

994 contribution to particulate pollution during haze events in China, Nature 514, 218–222,
995 https://doi.org/10.1038/nature13774, 2014.

996 Huang, S. L., Rahn, K. A., Arimoto, R., Graustein, W. C., and Turekian, K. K.: Semiannual
997 cycles of pollution at Bermuda, J Geophys Res-Atmos, 104, 30309-30317, 1999.

998 Jickells, T. D., Knap, A., Church, T., Galloway, J., and Miller, J.: Acid-Rain on Bermuda,
999 Nature, 297, 55-57, https://doi.org/10.1038/297055a0, 1982.

1000 Kadko, D., and Prospero, J.: Deposition of Be-7 to Bermuda and the regional ocean:
1001 Environmental factors affecting estimates of atmospheric flux to the ocean, J Geophys Res-
1002 Oceans, 116, C02013, https://doi.org/10.1029/2010JC006629, 2011.
1003
1004 Kassomenos, P., Vardoulakis, S., Borge, R., Lumbreras, J., Papaloukas, C., Karakitsios, S.:
1005 Comparison of statistical clustering techniques for the classification of modelled atmospheric
1006 trajectories, Theoretical and Applied Climatology 102, 1–12, https://doi.org/10.1007/s00704-
1007 009-0233-7, 2010.

1008 Keene, W. C., Moody, J. L., Galloway, J. N., Prospero, J. M., Cooper, O. R., Eckhardt, S., and
1009 Maben, J. R.: Long-term trends in aerosol and precipitation composition over the western North
1010 Atlantic Ocean at Bermuda, Atmos Chem Phys, 14, 8119-8135, https://doi.org/10.5194/acp-14-
1011 8119-2014, 2014.

1012 Kim, Y., Sievering, H., and Boatman, J.: Volume and surface area size distribution, water mass
1013 and model fitting of GCE/CASE/WATOX marine aerosols, Global Biogeochem Cy, 4, 165-177,
1014 https://doi.org/10.1029/GB004i002p00165, 1990.

1015 Knop, I., Bansmer, S.E., Hahn, V., Voigt, C.: Comparison of different droplet measurement
1016 techniques in the Braunschweig Icing Wind Tunnel, Atmospheric Measurement Techniques, 14,
1017 1761–1781, https://doi.org/10.5194/amt-14-1761-2021, 2021.

1018 Lawson, R.P., O'Connor, D., Zmarzly, P., Weaver, K., Baker, B., Mo, Q., Jonsson, H.: The 2D-S
1019 (Stereo) Probe: Design and Preliminary Tests of a New Airborne, High-Speed, High-Resolution
1020 Particle Imaging Probe, Journal of Atmospheric and Oceanic Technology 23, 1462–1477,
1021 https://doi.org/10.1175/jtech1927.1, 2006.

1022 Li, Q., Jacob, D. J., Fairlie, T. D., Liu, H., Martin, R. V., and Yantosca, R. M.: Stratospheric
1023 versus pollution influences on ozone at Bermuda: Reconciling past analyses, J. Geophys. Res.,
1024 107, 4611, https://doi.org/10.1029/2002JD002138, 2002.
1025
1026 Lin, J. T., and McElroy, M. B.: Impacts of boundary layer mixing on pollutant vertical profiles in
1027 the lower troposphere: Implications to satellite remote sensing, Atmos. Environ., 44(14), 1726–
1028 1739, https://doi.org/10.1016/j.atmosenv.2010.02.009, 2010.

1029 Lin, S.-J., and Rood, R. B.: Multidimensional Flux-Form Semi-Lagrangian Transport Schemes,
1030 Mon Weather Rev, 124, 2046-2070, https://doi.org/10.1175/1520-
1031 0493(1996)124<2046:MFFSLT>2.0.CO;2, 1996.

1032   Liu, H., Jacob, D. J., Bey, I. and Yantosca, R. M.: Constraints from ^{210}Pb and [7]Be on wet
1033   deposition and transport in a global three-dimensional chemical tracer model driven by
1034   assimilated meteorological fields, J. Geophys. Res. Atmos., 106(D11), 12109–12128,
1035   https://doi.org/10.1029/2000JD900839, 2001.

1036   Luan, Y., Jaeglé, L.: Composite study of aerosol export events from East Asia and North
1037   America, Atmospheric Chemistry and Physics, 13, 1221–1242, https://doi.org/10.5194/acp-13-
1038   1221-2013, 2013.

1039   Luo, G., Yu, F., and Schwab, J.: Revised treatment of wet scavenging processes dramatically
1040   improves GEOS-Chem 12.0.0 simulations of surface nitric acid, nitrate, and ammonium over the
1041   United States, Geosci. Model Dev., 12, 3439–3447, https://doi.org/10.5194/gmd-12-3439-2019,
1042   2019.

1043   Matsui, H., Kondo, Y., Moteki, N., Takegawa, N., Sahu, L.K., Zhao, Y., Fuelberg, H.E.,
1044   Sessions, W.R., Diskin, G., Blake, D.R., Wisthaler, A., Koike, M.: Seasonal variation of the
1045   transport of black carbon aerosol from the Asian continent to the Arctic during the ARCTAS
1046   aircraft campaign, Journal of Geophysical Research: Atmospheres 116, D05202,
1047   https://doi.org/10.1029/2010jd015067, 2011.

1048   Mead, C., Herckes, P., Majestic, B. J., and Anbar, A. D.: Source apportionment of aerosol iron in
1049   the marine environment using iron isotope analysis, Geophys Res Lett, 40, 5722-5727,
1050   https://doi.org/10.1002/2013GL057713, 2013.

1051   Merrill, J. T.: Isentropic Air-Flow Probability Analysis, J Geophys Res-Atmos, 99, 25881-
1052   25889, https://doi.org/10.1029/94JD02211, 1994.
1053
1054   Miller, J. M., and Harris, J. M.: The Flow Climatology to Bermuda and Its Implications for
1055   Long-Range Transport, Atmos Environ, 19, 409-414, https://doi.org/10.1016/0004-
1056   6981(85)90162-3, 1985.

1057   Milne, P. J., Prados, A. I., Dickerson, R. R., Doddridge, B. G., Riemer, D. D., Zika, R. G.,
1058   Merrill, J. T., and Moody, J. L.: Nonmethane hydrocarbon mixing ratios in continental outflow
1059   air from eastern North America: Export of ozone precursors to Bermuda, J Geophys Res-Atmos,
1060   105, 9981-9990, https://doi.org/10.1029/1999JD901117, 2000.
1061
1062   Moody, J. L., and Galloway, J. N.: Quantifying the relationship between atmospheric transport
1063   and the chemical composition of precipitation on Bermuda, Tellus B: Chemical and Physical
1064   Meteorology, 40, 463-479, https://doi.org/10.3402/tellusb.v40i5.16014, 1988.

1065   Moody, J. L., Oltmans, S. J., Levy II, H., and Merrill, J. T.: A transport climatology of
1066   tropospheric ozone, Bermuda: 1988–1991, J. Geophys. Res., 100, 7179-7194,
1067   https://doi.org/10.1029/94JD02830, 1995.
1068
1069   Moody, J. L., Keene, W. C., Cooper, O. R., Voss, K. J., Aryal, R., Eckhardt, S., Holben, B.,
1070   Maben, J. R., Izaguirre, M. A., and Galloway, J. N.: Flow climatology for physicochemical

1071   properties of dichotomous aerosol over the western North Atlantic Ocean at Bermuda, Atmos
1072   Chem Phys, 14, 691-717, https://doi.org/10.5194/acp-14-691-2014, 2014.

1073   Moteki, N., Kondo, Y., Oshima, N., Takegawa, N., Koike, M., Kita, K., Matsui, H., and Kajino,
1074   M.: Size dependence of wet removal of black carbon aerosols during transport from the
1075   boundary layer to the free troposphere, Geophys Res Lett, 39, L13802,
1076   https://doi.org/10.1029/2012GL052034, 2012.

1077   Muhs, D. R., Budahn, J. R., Prospero, J. M., Skipp, G., & Herwitz, S. R.: Soil Genesis on the
1078   Island of Bermuda in the Quaternary: The Importance of African Dust Transport and Deposition,
1079   Journal of Geophysical Research-Earth Surface, 117, F03025,
1080   https://doi.org/10.1029/2012JF002366, 2012.

1081   Nogueira, M.: Inter-comparison of ERA-5, ERA-interim and GPCP rainfall over the last
1082   40 years: Process-based analysis of systematic and random differences, Journal of Hydrology
1083   583, 124632, https://doi.org/10.1016/j.jhydrol.2020.124632, 2020.

1084   Oltmans, S. J., and Levy, H.: Seasonal Cycle of Surface Ozone over the Western North-Atlantic,
1085   Nature, 358, 392-394, https://doi.org/10.1038/358392a0, 1992.

1086   Oshima, N., Kondo, Y., Moteki, N., Takegawa, N., Koike, M., Kita, K., Matsui, H., Kajino, M.,
1087   Nakamura, H., Jung, J. S., and Kim, Y. J.: Wet removal of black carbon in Asian outflow:
1088   Aerosol Radiative Forcing in East Asia (A-FORCE) aircraft campaign, Journal of Geophysical
1089   Research: Atmospheres, 117, D03204, https://doi.org/10.1029/2011JD016552, 2012.

1090   Painemal, D., Corral, A. F., Sorooshian, A., Brunke, M. A., Chellappan, S., Afzali Gorooh, V.,
1091   Ham, S.-H., O'Neill, L., Smith Jr, W. L., Tselioudis, G., Wang, H., Zeng, X., and Zuidema, P.:
1092   An Overview of Atmospheric Features Over the Western North Atlantic Ocean and North
1093   American East Coast—Part 2: Circulation, Boundary Layer, and Clouds, Journal of Geophysical
1094   Research: Atmospheres, 126, e2020JD033423, https://doi.org/10.1029/2020JD033423, 2021.

1095   Park, R.J., Jacob, D.J., Palmer, P.I., Clarke, A.D., Weber, R.J., Zondlo, M.A., Eisele, F.L.,
1096   Bandy, A.R., Thornton, D.C., Sachse, G.W., Bond, T.C: Export efficiency of black carbon
1097   aerosol in continental outflow: Global implications, Journal of Geophysical Research:
1098   Atmospheres 110, D11205, https://doi.org/10.1029/2004jd005432, 2005.

1099   Prados, A. I., Dickerson, R. R., Doddridge, B. G., Milne, P. A., Moody, J. L., and Merrill, J. T.:
1100   Transport of ozone and pollutants from North America to the North Atlantic Ocean during the
1101   1996 Atmosphere/Ocean Chemistry Experiment (AEROCE) intensive, J Geophys Res-Atmos,
1102   104, 26219-26233, https://doi.org/10.1029/1999JD900444, 1999.

1103   Quan, J., Liu, Q., Li, X., Gao, Y., Jia, X., Sheng, J., Liu, Y.: Effect of heterogeneous aqueous
1104   reactions on the secondary formation of inorganic aerosols during haze events. Atmospheric
1105   Environment 122, 306–312, https://doi.org/10.1016/j.atmosenv.2015.09.068, 2015.

1106   Rolph, G., Stein, A., Stunder, B.: Real-time Environmental Applications and Display sYstem:
1107   READY, Environmental Modelling & Software 95, 210–228,
1108   https://doi.org/10.1016/j.envsoft.2017.06.025, 2017.

Schuster, G. L., Dubovik, O., and Holben, B. N.: Angstrom exponent and bimodal aerosol size distributions, Journal of Geophysical Research: Atmospheres, 111, D07207, https://doi.org/10.1029/2005JD006328, 2006.

Silva, S. J., Ridley, D. A., and Heald, C. L.: Exploring the Constraints on Simulated Aerosol Sources and Transport Across the North Atlantic With Island-Based Sun Photometers, Earth Space Sci, 7, e2020EA001392, https://doi.org/10.1029/2020EA001392, 2020.

Sinnott, R. W.: Virtues of the haversine, Sky and Telescope, Vol.68, No.2, p.159, 1984.

Sorooshian, A., Anderson, B., Bauer, S. E., Braun, R. A., Cairns, B., Crosbie, E., . . . Zuidema, P.: Aerosol–Cloud–Meteorology Interaction Airborne Field Investigations: Using Lessons Learned from the U.S. West Coast in the Design of ACTIVATE Off the U.S. East Coast, Bulletin of the American Meteorological Society, 100(8), 1511-1528, https://doi.org/10.1175/bams-d-18-0100.1, 2019.

Sorooshian, A., Corral, A. F., Braun, R. A., Cairns, B., Crosbie, E., Ferrare, R., . . . Zuidema, P.: Atmospheric Research over the Western North Atlantic Ocean Region and North American East Coast: A Review of Past Work and Challenges Ahead, Journal of Geophysical Research: Atmospheres, 125(6), e2019JD031626, https://doi.org/10.1029/2019JD031626, 2020.

Stein, A.F., Draxler, R.R., Rolph, G.D., Stunder, B.J.B., Cohen, M.D., Ngan, F.: NOAA's HYSPLIT Atmospheric Transport and Dispersion Modeling System. Bulletin of the American Meteorological Society 96, 2059–2077, https://doi.org/10.1175/bams-d-14-00110.1, 2015.

Stohl, A., Wotawa, G., Seibert, P., Kromp-Kolb, H.: Interpolation Errors in Wind Fields as a Function of Spatial and Temporal Resolution and Their Impact on Different Types of Kinematic Trajectories. Journal of Applied Meteorology 34, 2149–2165, https://doi.org/10.1175/1520-0450(1995)034<2149:ieiwfa>2.0.co;2, 1995.

Su, L., Yuan, Z., Fung, J.C.H., Lau, A.K.H.: A comparison of HYSPLIT backward trajectories generated from two GDAS datasets. Science of The Total Environment, 506-507, 527–537, https://doi.org/10.1016/j.scitotenv.2014.11.072, 2015.

Sun, Q., Miao, C., Duan, Q., Ashouri, H., Sorooshian, S., Hsu, K.: A Review of Global Precipitation Data Sets: Data Sources, Estimation, and Intercomparisons. Reviews of Geophysics 56, 79–107, https://doi.org/10.1002/2017rg000574, 2018.

Todd, D. L., Keene, W. C., Moody, J. L., Maring, H., and Galloway, J. N.: Effects of wet deposition on optical properties of the atmosphere over Bermuda and Barbados, J Geophys Res-Atmos, 108(D3), 4099, https://doi.org/10.1029/2001jd001084, 2003.

Tunved, P., Ström, J., and Krejci, R.: Arctic aerosol life cycle: linking aerosol size distributions observed between 2000 and 2010 with air mass transport and precipitation at Zeppelin station, Ny-Ålesund, Svalbard, Atmos. Chem. Phys., 13, 3643–3660, https://doi.org/10.5194/acp-13-3643-2013, 2013.

1145 US-EPA: Compendium of Methods for the de-termination of inorganic compounds in
1146 ambient air, USEPA/625/R-96/010a, United States Environmental Protection Agency,
1147 Washington, D.C., 1999.

1148 Veron, A. J., Church, T. M., Patterson, C. C., Erel, Y., and Merrill, J. T.: Continental Origin and
1149 Industrial Sources of Trace-Metals in the Northwest Atlantic Troposphere, J Atmos Chem, 14,
1150 339-351, https://doi.org/10.1007/BF00115243, 1992.

1151 Wang, Q., Jacob, D. J., Fisher, J. A., Mao, J., Leibensperger, E. M., Carouge, C. C., Le Sager, P.,
1152 Kondo, Y., Jimenez, J. L., Cubison, M. J., Doherty, S. J., Sager, P. Le, Kondo, Y., Jimenez, J. L.,
1153 Cubison, M. J., and Doherty, S.J.: Sources of carbonaceous aerosols and deposited black carbon
1154 in the Arctic in winter-spring: implications for radiative forcing, Atmos. Chem. Phys., 11(23),
1155 12453–12473, https://doi.org/10.5194/acp-11-12453-2011, 2011, 2011.

1156 Wang, Y.Q., Zhang, X.Y., Draxler, R.R.: TrajStat: GIS-based software that uses various
1157 trajectory statistical analysis methods to identify potential sources from long-term air pollution
1158 measurement data, Environmental Modelling & Software, 24, 938–939,
1159 https://doi.org/10.1016/j.envsoft.2009.01.004, 2009.

1160 Weinstock, B.: Carbon Monoxide: Residence Time in the Atmosphere, 166, 224–225,
1161 https://doi.org/10.1126/science.166.3902.224, 1969.

1162 Wesely, M. L.: Parameterization of surface resistances to gaseous dry deposition in regional-
1163 scale numerical models, Atmospheric Environment (1967), 23, 1293-1304,
1164 https://doi.org/10.1016/0004-6981(89)90153-4, 1989.

1165 Wolff, G. T., Ruthkosky, M. S., Stroup, D. P., Korsog, P. E., Ferman, M. A., Wendel, G. J., and
1166 Stedman, D. H.: Measurements of SOx, NOx and Aerosol Species on Bermuda, Atmos Environ,
1167 20, 1229-1239, https://doi.org/10.1016/0004-6981(86)90158-7, 1986.

1168 Wu, S., Mickley, L. J., Jacob, D. J., Logan, J. A., Yantosca, R. M. and Rind, D. Why are there
1169 large differences between models in global budgets of tropospheric ozone?, J. Geophys. Res.
1170 Atmos., 112(D5), 1–18, https://doi.org/10.1029/2006JD007801, 2007.

1171 Yu, H., Yang, Y., Wang, H., Tan, Q., Chin, M., Levy, R.C., Remer, L.A., Smith, S.J., Yuan, T.,
1172 Shi, Y.: Interannual variability and trends of combustion aerosol and dust in major continental
1173 outflows revealed by MODIS retrievals and CAM5 simulations during 2003–2017, Atmospheric
1174 Chemistry and Physics, 20, 139–161, https://doi.org/10.5194/acp-20-139-2020, 2020.

1175 Yu, K., Keller, C. A., Jacob, D. J., Molod, A. M., Eastham, S. D. and Long, M. S.: Errors and
1176 improvements in the use of archived meteorological data for chemical transport modeling: an
1177 analysis using GEOS-Chem v11-01 driven by GEOS-5 meteorology, Geosci. Model Dev., 11,
1178 305–319, https://doi.org/10.5194/gmd-2017-125, 2018.

1179 Zhang, B., Liu, H., Crawford, J. H., Chen, G., Fairlie, T. D., Chambers, S., Kang, C.-H.,
1180 Williams, A. G., Zhang, K., Considine, D. B., Sulprizio, M. P., and Yantosca, R. M.: Simulation
1181 of radon-222 with the GEOS-Chem global model: emissions, seasonality, and convective
1182 transport, Atmos. Chem. Phys., 21, 1861–1887, https://doi.org/10.5194/acp-21-1861-2021, 2021.